Title

Anode-Design Strategies for Improved Performance of Polymer-Electrolyte Fuel Cells with Ultra-Thin Electrodes

Permalink

https://escholarship.org/uc/item/7cs219ph

Journal

Joule, 2(7)

ISSN

2542-4785

Authors

Steinbach, Andrew J
Allen, Jeffrey S
Borup, Rodney L
et al.

Publication Date

2018-07-01

DOI

10.1016/j.joule.2018.03.022

Peer reviewed

Anode-design strategies for improved performance of polymer-electrolyte fuel cells with ultra-thin electrodes

A. J. Steinbach[a], J. S. Allen[g], R. L. Borup[b], D. S. Hussey[c], D. L. Jacobson[c], A. Komlev[a], A. Kwong,[d] J. MacDonald[d], R. Mukundan[b], M. J. Pejsa[a], M. Roos[d], A. D. Santamaria[d,f], J. M. Sieracki[a], D. Spernjak[b], I. V. Zenyuk[d,e] and A. Z. Weber[d]*

[a] 3M Company, Fuel Cell Components Program, 3M Center, St. Paul, MN 55144, USA
[b] Los Alamos National Laboratory, MS D429, MPA-11, Los Alamos, NM 87545
[c] NIST Center for Neutron Research, 100 Bureau Drive, MS 8461, Gaithersburg, MD 20899
[d] Lawrence Berkeley National Laboratory, 1 Cyclotron Rd, MS70-108B Berkeley, CA 94720
[e]Mechanical Engineering Department, Tufts University, 200 Boston Ave. 2600, Medford, MA 02155
[f]Mechanical Engineering Department, Western New England University, 1215 Wilbraham Road, Springfield, MA 01119
[g]Department of Mechanical Engineering – Engineering Mechanics, Michigan Technological University, 1400 Townsend Drive Houghton, MI 49931

We report results of systematic diagnostic and cell studies to elucidate the mechanistic role of the experimentally-determined influence of the anode gas diffusion layer (GDL) on the performance of ultra-thin electrode polymer-electrolyte fuel cells. Measurements of product water balance and *in-situ* neutron imaging of operational membrane-electrode-assembly (MEA) water profiles demonstrate how improved performance is observed due to a novel anode GDL fiber-density modulated structure at the micrometer scale that removes water preferentially out of the anode, a key strategy to manage water in these cells. The banded structure results in low transport-resistance pathways, which impact water-droplet removal from the GDL surface. This interfacial effect is unexpectedly shown to be critical for decreasing overall water holdup throughout the cell. These studies demonstrate a new material paradigm for understanding and controlling fuel-cell water management and related high-power technologies, and the need for systematic holistic studies.

(*) to whom correspondence should be addressed. E-mail: azweber@lbl.gov

Context and Scale

Very thin electrodes enable high power density, yet their thinness engenders issues related to buildup of products (e.g., water in polymer-electrolyte fuel cells (PEFCs)). The article explores an unexpected materials solution to the problem, which highlights the need to study such complicated systems in a holistic manner of a complete cell due to the nonlinearities existent in the highly coupled physical phenomena. The materials solution demonstrates the importance of backing layers in controlling PEFC water management. The improved performance is due to an inherent unintentional manufacturing heterogeneity, which mainly impacts its surface properties. With this knowledge, one can now engineer and optimize these critical heterogeneities for different architectures. The findings are relevant to those working on materials for electrochemical energy conversion, and they represent new key knowledge that can have significant impacts in PEFCs and related electrochemical cells.

Keywords: fuel cells; ultra-thin electrodes; water management; transport phenomena; material design

1. Introduction

Reducing expensive catalyst loadings is critical for the wide-spread implementation of polymer-electrolyte fuel-cell (PEFC) systems for a wide variety of applications. One method to do so is to utilize membrane-electrode-assemblies (MEAs) that have ultra-thin (< 1 µm) catalyst layers,[1-6] as explored by 3M in their nanostructured-thin-film (NSTF)[i] catalyst technology.[7-9] NSTF catalyst layers have several other demonstrated advantages compared to MEAs comprised of conventional, relatively thick (~10µm) carbon-supported catalysts, including increased durability towards start-stop and voltage cycling,[8] higher specific activity, and high specific rated power.[8,10] While this approach can meet the performance targets with low catalyst loadings at elevated operating temperatures, it is plagued by poor performance and startup at ambient conditions; a new material solution is required.[8] This is especially important as these intermediate temperature ranges are critical for successful startup, and also for short commutes or colder weather wherein the cell does not fully reach the elevated operating temperatures.

The reduced low-temperature performance can be attributed to the NSTF's much higher water generation rate per unit catalyst volume and to an electrode pore structure that is more susceptible to water condensation and flooding due to enhanced hydrophilicity of the extended Pt films.[9,11,12] Water-transport processes in PEFCs are shown schematically by **Figure S1**, where transport resistances due to finite permeability of liquid in the gas-diffusion layer (GDL) (R_{GDL}),

---

[i] Certain trade names and company products are mentioned in the text or identified in an illustration in order to adequately specify the experimental procedure and equipment used. In no case does such identification imply recommendation or endorsement by the National Institute of Standards and Technology, nor does it imply that the products are necessarily the best available for the purpose.

membrane (R_m) and interfacial GDL|channel ($R_{GDL|chan}$) are shown as well. A recent modeling study demonstrated that thinner catalyst layers are much more susceptible to flooding at low temperatures where phase-change-induced flow can no longer vaporize and transport most of the product water.[11] That numerical study suggested that GDL and membrane properties including interfacial resistances could help alleviate the water-management issue for PEFCs with thin catalyst layers.

It has been shown that the low-temperature performance of NSTF MEAs can be enhanced by changing cell operation or architecture,[13,14] but there is a lack of understanding of the critical properties that are being affected or controlling. For example, substantial gains in MEA maximum power output near room temperature were observed by operating the MEAs with reduced anode reactant pressures, including below atmospheric, but there are questions of practicality and mechanisms including key processes and locations being impacted. Product water-distribution measurements suggest that the increased performance with reduced anode operating pressure correlates with reduced liquid-water flowrate out of the cathode GDL, likely reducing liquid saturation levels in the cathode electrode and minimizing transport losses.[11,14,15] The anode GDL backing was also found to be highly influential; in experiments conducted with several different anode gas diffusion layer backings without MPLs, up to a 2 fold variation in the maximum current density was observed at 30°C.[13] Limited experimental results with two anode GDLs with modest performance variation indicated that the anode GDL did not substantially influence the water distribution as was the case with reduced anode operating pressure,[14] indicating that the mechanism of the anode GDL influence on low temperature response is unclear.

In this work, experiments are conducted to obtain further mechanistic insight into the role of the anode GDL backing on NSTF MEAs' performance sensitivity to operating temperature. Two types of GDLs were considered here that demonstrated significantly different low-temperature performance: MRC U105 and MRC C, where the remaining components of the PEFCs remained the same. This way individual contributions to the water-transport resistances due to anode GDL and GDL|channel interface (see Figure S1) can be elucidated. To understand the controlling phenomena and provide guidance for material developers, multiple *operando*, *in*- and *ex-situ* characterizations are conducted.

2. Results and Discussion

2.1. Cell Results

2.1.1. Polarization and Water Balance

Figure 1 summarizes the measured 80°C reference H_2/Air performance and temperature sensitivity for the MEAs with the MRC U105 and MRC C anode GDLs, where each data point is the mean of three consecutive experiments. Under reference operating conditions (Figure 1a), both MEAs had similar performance in the kinetic regime, but the cell voltage for MRC C is lower compared to MRC U105 at higher current densities, largely due to higher electrical resistance, as evidenced by the higher high-frequency resistance (HFR). The higher electrical resistance in MRC C is perhaps due to its structure as discussed later and in the SI. In terms of temperature sensitivity **(Figure 1b**), the MEA with the MRC C anode GDL is able to maintain a current density above 1 A cm^{-2} for temperatures down to 50°C, whereas for the MEA with the MRC U105 anode GDL, the current drops below 0.5 A cm^{-2} at 0.5 V for temperatures below 55ºC. Therefore, the MEA with MRC C was able to deliver a 4-fold increase in current density at 0.5 V and 50°C compared to that with the MRC U105 anode GDL (i.e., 1 and 0.26 Acm^{-2} at 50°C for MRC C and MRC U105, respectively). The results presented here are consistent in trend with those reported previously,[13,14] but are quite surprising in terms of magnitude and the fact that one is only changing the anode GDL, which is typically considered less important for overall PEFC performance than the cathode GDL.

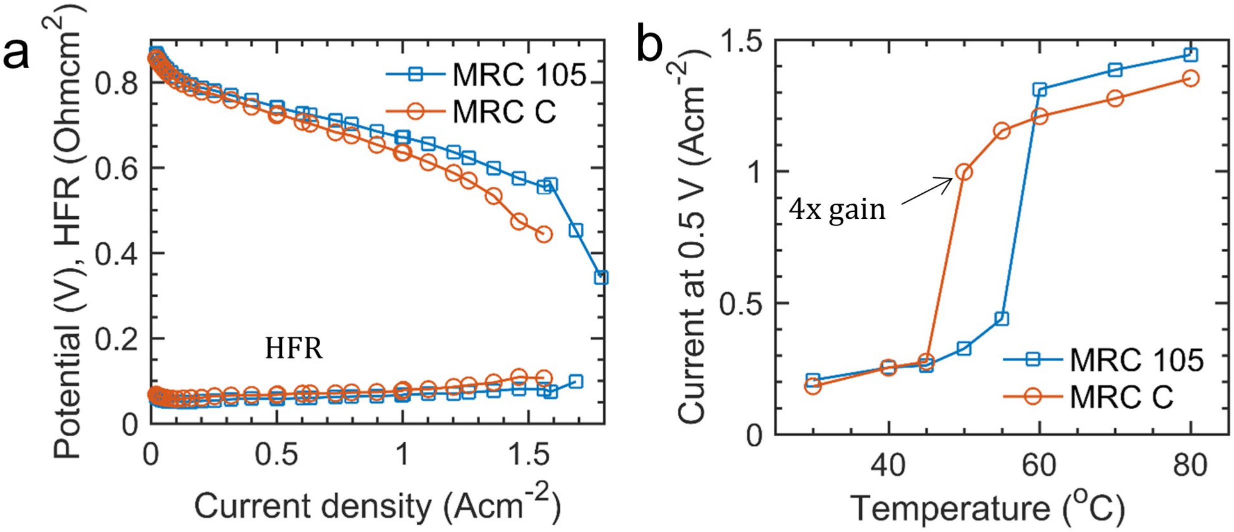

Figure 1. (a) Measured 80°C H_2/Air polarization curves and high-frequency resistance and (b) summarized temperature sensitivity for MEAs with either MRC U105 or “C” anode GDLs.

Figure 2a summarizes the measured polarization curves under the product water balance, temperature series measurements (Table S1, second row) with MEAs containing either the MRC U105 or MRC C based anode GDLs. At 60°C, MEAs with either anode GDL were able to achieve at least 1.2 A cm^{-2}. As the temperature was reduced towards 30°C with either MEA, the measured cell voltage at a given cell current density decreased, and the maximum current density achievable also decreased. However, the MEA with MRC C was able to generate substantially higher current densities than the MEA with MRC U105 anode at 40°C and 45°C, and cell voltages at 0.25 A cm^{-2} were higher between 50 and 30°C, which are key startup and perhaps operational points as noted above.

Insight into the mechanism of the large performance differences at intermediate and low cell temperatures can be ascertained by examining the fraction of product water that exits the anode effluent stream (**Figure 2b**). As the cell temperature decreased from 60°C, the fraction of product water that exited the cell out the anode effluent stream increased substantially, to approximately 40 % at 1 A cm^{-2} and 50 °C, in a similar fashion for both anode GDL types. As the cell operating temperature decreased from 50 to 35°C, the anode fraction of product water removal with MRC C increased further, to as high as about 60% at 0.25 A cm^{-2}, whereas with MRC U105 no further increase in anode product water removal fraction was observed. Thus, there is seemingly a plateau in the percentage of water that will leave the anode, and which is dominated by the anode GDL (see Figure S2 in SI). Furthermore, low-temperature performance is enhanced by increasing that percentage. These findings are consistent with the increasing the fraction out of the anode by lowering its pressure,[15] although here it is dominated by a material change.

The plateau in the performance as the limiting anode GDL water removal rate is approached can be more clearly seen by examining the performance of the two cells at a given current density (i.e., same water production rate) as a function of cell temperature. **Figure 3** directly compares the dependence of cell voltage at 0.25 Acm^{-2} to the fraction of product water removed out the anode for cells operated between 60 and 30°C for the MEAs with either MRC U105 or MRC C anode GDLs.

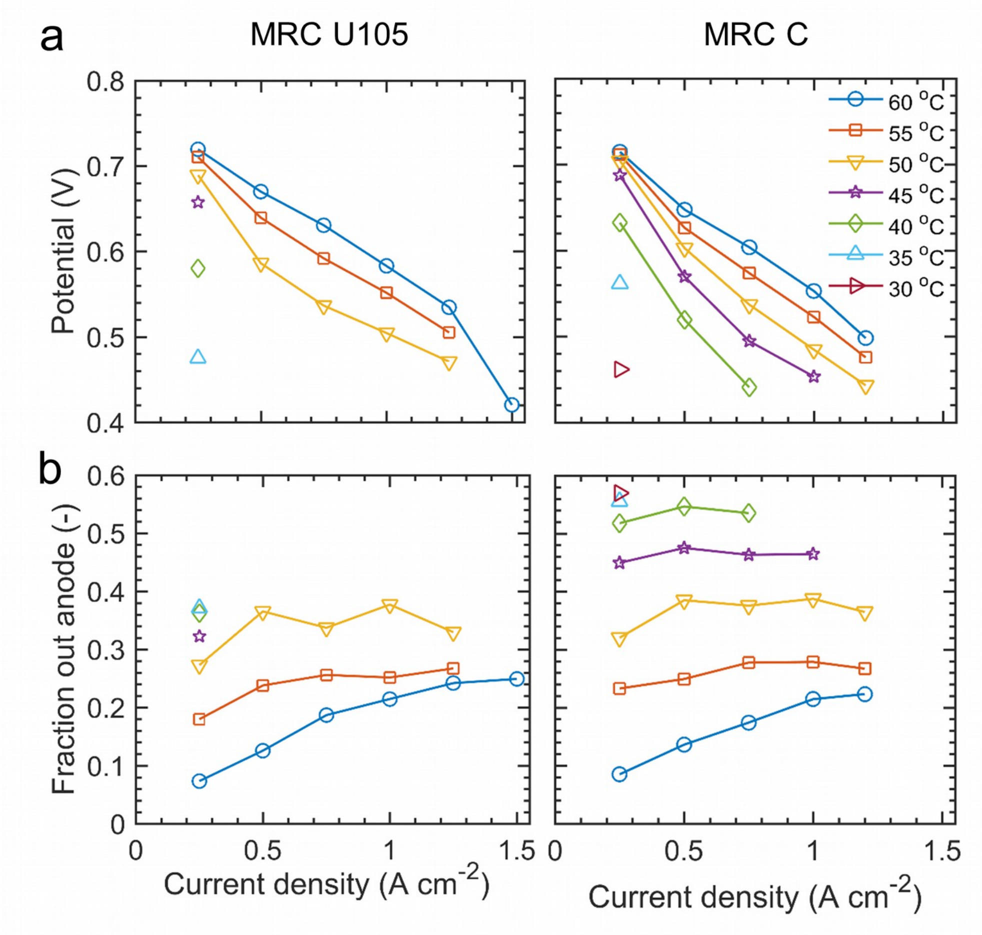

Figure 2. Measured cell voltage (a) and fraction of product water removed out of the anode (b) as a function of current density for different temperatures. Operating conditions were 1/1atm H_2/Air, constant stoichiometry 2/2, dry inlet gases, lines are a guide to the eye.

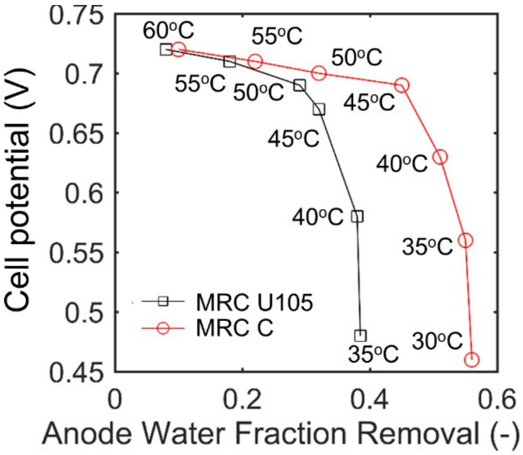

Figure 3 Cell potential at 0.25 Acm^{-2} as a function of anode water removal fraction for MRC U105 and MRC C for temperature range of 30 to 60°C.

At the maximum temperature of 60°C, both anode GDLs yield similar performance and anode removal fractions of around 10 %. The corresponding absolute anode water removal rate of ca. 0.1 $\mu Lcm^{-2}min^{-1}$ (Figure S2(b)) at 60°C is similar to the removal rate calculated for a vapor saturated effluent stream at the cell anode exit conditions. As the temperature decreased from 60 to 50°C, the measured cell voltage decreased relatively gradually and the anode water removal fraction increased for both anode GDL types, but the cell voltage and water removal fractions were modestly higher with MRC C than with MRC U105. As the temperature decreased to 45°C and lower, the cell voltage of the MRC U105 cell decreased more rapidly and the water removal fraction appeared to approach a limiting value of about 38%. In comparison, the MEA with the MRC C anode GDL also showed an apparent limiting water removal fraction, but the onset of rapid performance loss with the MRC C MEA did not occur until the cell temperature was cooled to 40°C and the limiting fraction was about 56%, which is about 47% higher than the MRC U105 anode GDL limiting removal fraction.

There is also an interplay between product water removal distributions between anode and cathode and cell temperature and pressure as shown in Figure S3 in the SI. The performance at moderate cell temperatures (40 and 50°C) is higher when the anode pressure is lower than the cathode pressure. The anode water removal fraction also was found to depend on anode pressure, with enhanced anode water removal fractions at lower anode pressure, consistent with expectation based on the analysis above. Additionally, as shown in Figure S4 in the SI, the calculated liquid water flux exiting the cell cathode also trends as expected for variation in anode GDL type and anode pressure. Overall, the water balance data is suggestive that substantial performance losses occur when the limiting anode water removal rate is reached, and that this limiting water removal rate depends upon properties of the anode GDL.

2.1.2. Neutron Imaging

To explore how more water out of the anode improves cell performance as well as the operation of the different anode GDLs, *operando* neutron imaging of the cells was done. For high resolution, as noted in the experimental section, small single-serpentine 2.5 cm^2 cells are required (which typically demonstrate lower performance than larger 50 cm^2 PEFC), whereas low-resolution imaging used the original 50 cm^2 quad-serpentine cells. (High-resolution data is shown in the paper and in SI, while the low-resolution data is shown in the SI.) A comparison of the water profiles measured at 80°C at 0.3 V for the two cells does not show a significant difference in terms of water amount in the layers or distribution (see **Figure 4**a). Both cells were operated at the same constant voltage in order to keep the heat generation constant and to prevent cell reversal at constant-current operation. More details about heat generation and water transport in these small cells are provided in reference [16]. At constant voltage, the cell with the MRC U105 anode GDL had slightly lower current and hence lower water production. The profile shows a second peak in water saturation at the cathode GDL/cathode channel edge indicating liquid water removal from the cathode substrate into the channel is critical in determining the MEA water content at low operating voltages and high currents, which also demonstrates phase-change-induced flow under these conditions.[17-19] The impedance plots shown in Figure 4c illustrate that the cell with the MRC C GDL has a higher high frequency resistance (0.06 Ω cm^2 compared to 0.04 Ω cm^2) than the cell with the MRC U105 GDL when operated at 80°C, consistent with the 50 cm^2 cell data described in Figure 1a above. However, the cell using the MRC C anode GDL has a 50 % reduction in the low frequency resistance (0.2 Ω cm^2 compared to 0.4 Ω cm^2). This decreased mass-transport resistance is associated with the lower observed MEA water content and correlates with improvement in cell performance. This also illustrates that these smaller cells are more sensitive to changes in water content than conventional 50 cm^2 cells where little anode GDL effect was seen while operating at elevated temperatures.

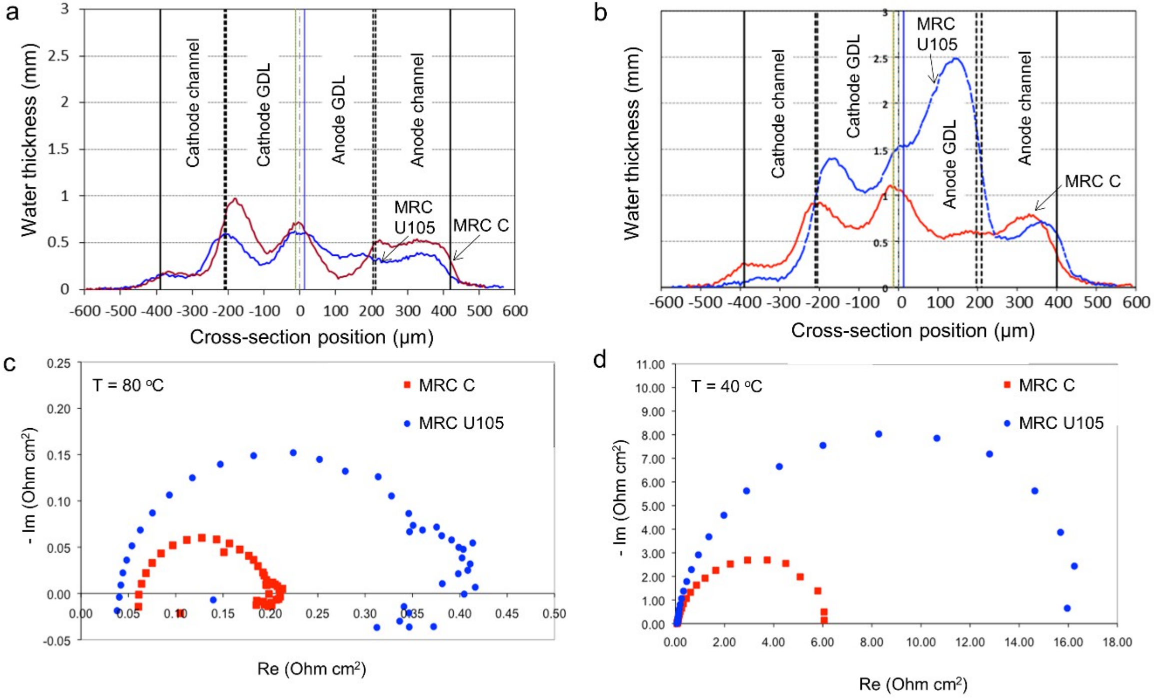

Figure 4. Comparison of water distribution and electrochemical impedance spectra (EIS) in operating high-resolution imaging fuel cells using MRC U105 and MRC C anode GDLs, at high and low operating cell temperature. (a) Water profiles (thickness of integrated water amount) measured at 0.3V and 80°C. (b) Water profiles measured at 0.3V and 40°C. (c) EIS at 80°C and 1.2 Acm^{-2}. (d) EIS at V = 0.3 V and current densities of 0.1 for MRC U105 and 0.42 Acm^{-2} for MRC C.

Of more interest, are the water profiles and impedance of the two cells operated at 40°C (Figure 4b and d). As can be seen in Figure 4b, the water amount is higher than with the higher temperature operation, in agreement with evaporation and associated transport at higher temperatures.[19-23] This is also witnessed in a larger cell with the low-resolution imaging (see Figure S7 in SI). In terms of comparison, the cell with MRC U105 anode GDL is overall higher than that in the MRC C one, in agreement with its worse performance at all current densities as shown in SI. From the high-resolution imaging in Figure 4c, it is apparent that there is 40% less water in the MEA and cathode GDL with the MRC C anode cell. The extra water in the cell with MRC U105 results in a 4 times lower limiting current, probably mainly due to the oxygen electrode (i.e., less flooding causing oxygen limitations). Furthermore, while the cell with the MRC U105 anode GDL shows a water peak in the anode GDL, the cell with the MRC C GDL has a flatter profile with five times lower liquid water amount in the anode GDL. This suggests that perhaps the water retention in the anode GDL is important in terms of the water retention in the cell, which also agrees with the water analysis described above. It also could be due to a higher resistance of droplet removal into the gas channel, also marked by resistances R_{GDL}, a and $R_{GDL|Ch}$ in Figure S1.

2.2. GDL Characterization

It is apparent that the performance difference in the cells is related to the anode GDL in terms of its ability to reduce the overall water content in the cell, and specifically the MEA and probably cathode catalyst layer. To explore the key phenomena and properties that cause this, the two anode GDLs were analyzed with *ex*- and *in-situ* tests (see Table S2 for material-property differences).

2.2.1. Transport Properties

To discern the key phenomena, various characterizations were accomplished on the two different GDLs. It should be noted that the error bars in Figure 5 and the analysis in Figures S13, S14, S16, S17 demonstrate that the identified changes discussed herein are statistically relevant. As noted above, the higher-temperature performance of cells with MRC C were not as good as those with MRC U105. The reason for this is shown in **Figure 5**a, where MRC C has on average 1.6 to 1.8 times higher thermal conductivity and also higher thermal contact resistance, resulting in a slightly higher overall thermal resistance. The increased thermal contact resistance is consistent with the impedance data that shows increased electrical contact resistance for the cells using MRC C GDL. For water removal, it might be desirable to have a GDL with a lower thermal conductivity to ensure larger thermal gradients to drive water via evaporation and phase-change-induced flow, a mechanism whose effectiveness decreases with operating temperature due to the exponential nature of water vapor pressure with temperature.[17,19,21] Generally, it is also desirable to reduce contact resistance between the GDL and bipolar plate for effective heat removal as this is where most of the heat is removed in the cell. At larger compressions, the thermal contact resistance is more than 2 times larger for MRC C compared to MRC U105.

This impact of compression is evident in Figure 5b, which shows compressive, through-plane stress-strain curves for the GDLs. MRC C is more easily deformable compared to MRC U105, which is probably due its inherent structure and slightly higher porosity. For MRC U105, a linear regime is observed for a strain from 0 to 0.08, whereas for MRC C, the linear regime was observed for a longer range of strains up to 0.2. At 1 MPa of stress MRC C will deform 4 times more than MRC U105. Linear fits were created to fit these data points to extract Young's Modulus. For MRC C it was 1.6 MPa, whereas for MRC U105 it was 5.9 MPa, amounting to the ratio between the two of 3.7. For structural stability and PEFC durability, it is desirable to have GDLs that can sustain stress without much deformation (i.e., large Young's modulus); although MRC C minimizes water-management issues, its durability remains to be studied.

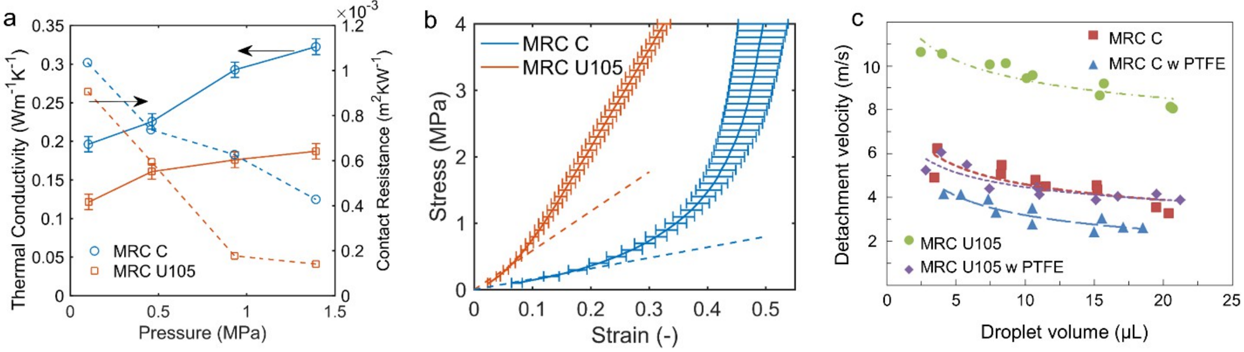

Figure 5 (a) Thermal conductivity and contact resistances for a range of compression pressures and (b) Stress-strain curves for MRC U105 and MRC C. (c) Droplet detachment velocity as a function of droplet volume for MRC U105 and MRC C GDLs with and without PTFE.

The difference in porosity and deformability is expected to cause changes to the water-retention or water-saturation curves. However, significant differences were not observed (see Figure S10 and S17 in SI) although they are not identical in the steep part of the curve. Thus, the minor differences in the water-retention curves could perhaps cause some of the changes in the observed saturations, but these are not believed to describe the performance differences as the anode saturation is not limiting and saturation is not necessarily correlated strongly to water movement. The MRC C GDL is a bit more hydrophobic in character, which explains partially the observed water-saturation profiles from the high-resolution neutron imaging (see Figure 4). However, it also does have a slightly higher residual saturation, meaning that the impact at higher temperatures is probably not as strong, which agrees with the experimental performance data. Similar to the above small differences, the effective gas diffusivities of the two different GDLs are likewise similar (see Figure S11 in SI), with the MRC C having higher normalized effective diffusivity values compared to MRC U105. These findings are in agreement with HFR data shown above and support argument that MRC C has overall lower mass-transport resistance compared to MRC U105 for the same level of liquid-water saturation. Lower mass-transport resistance can help in water removal from the CL in form vapor via phase-change induced flow. However, at low temperatures the evaporative mechanism is suppressed.

All of the above tests did not find larger deviations in properties that can explain the much better low-temperature performance of the cell with the MRC C anode GDL. However, when testing the droplet detachment velocities, a significant difference is noticed between the GDLs as shown in **Figure 5c**. The detachment velocity is indicative of the gas velocity needed to remove a certain size droplet from the GDL surface that was formed through liquid-water injection through the GDL. The higher the detachment velocity, the larger the droplet’s resistance to removal. Thus, a GDL with a smaller detachment velocity means that there are more and smaller droplets that detach sooner, resulting in an easier way to remove the water (and gases to flow in the channel), which is associated with lower liquid pressure compared to the higher detachment-velocity case.[11] This result stems from the different interactions of water emergence, underlying structure, surface pinning, etc.[24] This change is also consistent with time-averaged profiles seen in experiments.[25] An increased liquid pressure at the boundary should result in higher retained water throughout the cell.[24,26] From Figure S1, the interfacial GDL droplet removal resistance can be as relevant as internal GDL resistance, similar to the thermal properties. Both pristine MRC U105 and that with PTFE show higher detachment velocity compared to MRC C for all droplet volumes. The highest detachment velocity is observed for the smallest droplets of liquid (3 μL). Both MRC layers showed lower droplet detachment velocities at all droplet sizes when coated with PTFE. When no PTFE is present water clusters within the GDLs form connected networks and feed water droplets in the channel, thus having stronger droplet adherence to the surface of the GDL. This detachment velocity was associated with increased cell performance previously, especially with regards due to changes with PTFE content and aged samples.[26]

Table 1 summarizes the characterization findings for the MRC U105 and MRC C properties. To remove water from cathode into the anode channel at low temperatures it is desirable for the anode GDL to have both high permeability (low $R_{GDL,a}$ from Figure S1) and low droplet detachment velocity (low $R_{GDL|ch,a}$ from Figure S1). At the same time, the anode GDL has to be structurally stable and allow for hydrogen delivery. By tailoring a GDL's morphology, such a benefit could be realized. Furthermore, it appears that the beneficial effect of MRC C is also due to its interfacial transport properties more so than bulk ones.

Table 1. Property comparison table between MRC U105 and MRC C where shading denotes the significance of the change and green is better than orange.

	MRC U105	MRC C	Implication
High-frequency EIS resistance	🟩 Lower	🟧 Higher	Contact resistance scaling with high-frequency EIS

Thermal conductivity	Lower	Higher	Heat removal enhanced with thermal conductivity increase
Young’s Modulus	Higher	Lower	Stronger material with higher modulus
Effective gas diffusivity	Slightly lower	Slightly higher	Impact of saturation on gas transport
Porosity	Slightly Lower	Slightly Higher	Scales with liquid permeability
Water retention curve	Slightly Lower	Slightly Higher	Saturation filling as a function of pressure
Droplet detachment velocity	Higher	Lower	Ability to remove droplets from the surface of the GDL

2.2.2 Structural Properties

To examine the structure and explain the *ex-situ* and *operando* findings, imaging is conducted. As shown by **Figure 6**a and b, initial backlight projections (see Figure S9 in SI for higher magnifications) demonstrate that while MRC U105 appears uniform, MRC C contains fiber-density modulations (i.e., regions of higher and lower fiber contents). This was surprising as these novel GDLs were not engineered to contain such modulations. The optical backscattering is confirmed with more detailed investigations using x-ray computed tomography as shown in Figure 6c and d. The data reveals that MRC C has channels of low fiber density alternating with patches of high fiber density that are 340 μm in width, whereas fibers in MRC U105 do not have preferential orientation. This is also seen in the specific pore-size distributions of these materials and regions shown in Figures S13-S15 as discussed in the SI. *In-situ* studies demonstrate that water preferentially exists in the low density regions (see **Figure 6e-h**). The reconstructed and segmented tomographs at the centerline of the sample are shown too for the highest liquid pressures at breakthrough. Again, it is apparent that the fiber-density modulations seemingly design preferential channels for water transport. Such an impact has been engineering previously using radiation grafting[27] and laser perforating or milling GDLs and/or MPLs before,[28-39] but not with a materials solution on a micrometer lengthscale as observed here. Thus, we have defined a design strategy that micrometer modulations, which also does not necessitate precise alignment with flowfields as the previous studies can require.

For liquid pressures lower than 0.5 kPa, MRC C GDL exhibits liquid-water saturation at all locations of lower than 0.2, whereas for MRC U105 it is higher than 0.4 at the center of the sample, which agrees qualitatively with the water-retention behavior (see Figure S10 in SI). At 0.49 kPa, a breakthrough-pressure is already observed for MRC U105. For MRC C, mostly regions with high porosity at and near the interface with the sample stage become saturated at low pressures. A sharp transition in saturation profile for MRC C occurs at liquid pressures higher than 0.5 kPa, with large saturation values corresponding to higher porosity regions. **Figure 6**e and f show 3D volume-rendered water tomographs at a pressure of 0.55 and 0.49 kPa for MRC C and MRC U105, respectively. The regions of fiber-density modulation are mostly present at and near the top of the MRC C surface. To reach these regions, water has to overcome a more homogeneous structural fibrous layer that precedes the fiber-density modulated regions. The waviness of the water front is clearly observed for MRC C, whereas for MRC U105 water distribution is not directional. This waviness at the surface no doubt contributes to the lower detachment velocity (and higher contact resistance), since the water droplets emerge from domains that have less fibers and thus less pinning [18, 19].

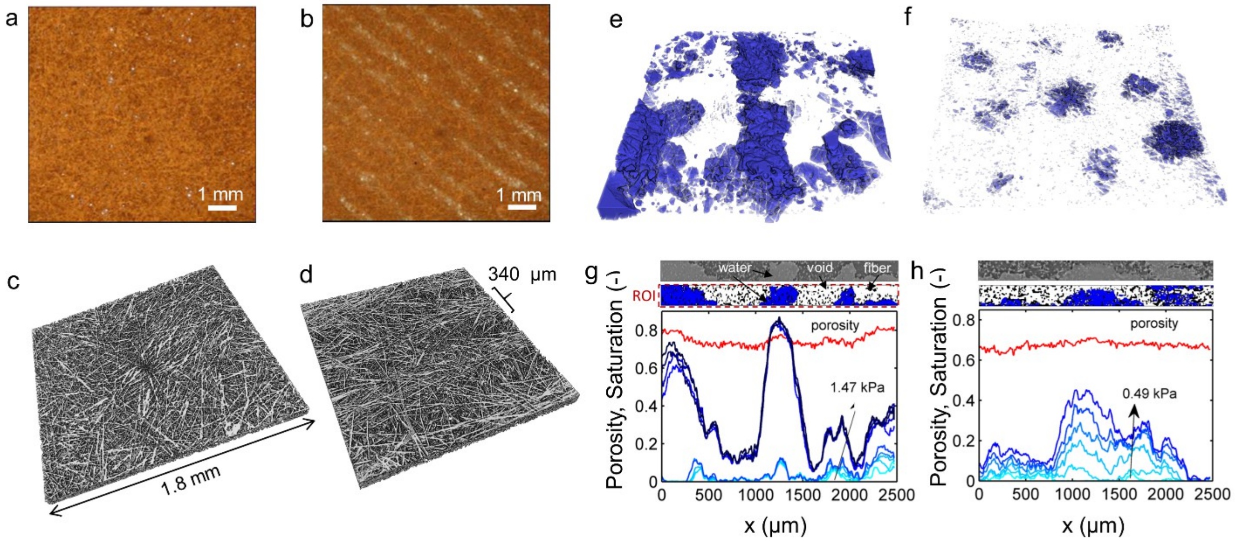

Figure 6. Optical micrographs of a) MRC U105 an b) MRC C. X-ray CT of c) MRC U105 and d) MRC C. Fiber-density modulated regions are shown in b) and d), where on average a 340 μm region of dense fibers was observed periodically. Volume-rendered liquid water for e) MRC C at 0.55 kPa and f) MRC U105 at 0.49 kPa liquid pressure. Area-averaged cross-section porosity and liquid saturation at different liquid injection pressures for g) MRC C and h) MRC U105. The raw tomographs and segmented images are shown on top, where water, void and fiber are marked; These values were computed as cross-sectional area-averaged properties for the in-plane direction. The region of interest (ROI) is also shown.

The MRC C GDL also had a higher calculated porosity (0.75) compared to that for MRC U105 (0.67), which agrees with the stress-strain data. At all levels of compression, it appears that MRC C has higher porosity by about 0.05 (see Figures S13-S16 and the SI for a more detailed discussion on porosity). As **Figure 6g** shows, the porosity distribution of MRC C has waviness to it with the difference between the high- and low-fiber density regions amounting to 0.08 to 0.06. Upon compression, the porosity difference between the bands of high and low fiber densities is preserved as shown in Figure S12. The porosity of MRC U105 is more uniform, as this material is more isotropic, which was also shown by **Figure 6** and supported by Figure S12. The modulation and compression and their impact on overall water uptake is also observed in Figure S17, where the saturation profiles from the XCT images are examined for different specific regions within the GDLs.

Overall, the complex morphology and interfacial properties of the MRC C GDL allows for enhanced water removal and thus more water out of the anode and better performance. These findings highlight the importance that the interface plays in controlling overall PEFC water management, as well as pathway for a materials solution for ultra-thin catalyst layers. Specifically, fiber-density modulations on the relative order of at least 10 to 20% can be used to provide preferential water pathways and subsequent easier removal of water droplets. Such effects were also seen in a previous ex-situ study for water within GDLs[40] as well as with another GDL (see Figure S18), where again one can correlate improved performance with the modulations and water pathways and subsequent lowering of the droplet detachment velocity, thus helping to establish the generality of the above findings.

3. Summary

For fuel cells to be commercialized, new material solutions are required to enable high performance at low loadings of expensive catalyst material. One strategy for this is to use nanostructured thin-film catalyst layers. As discussed in this paper, the current water-management limitations of these thin films can be overcome through novel materials, and surprisingly, by the gas-diffusion layer (GDL) on the anode side of the cell. The improved anode GDL allows a higher fraction of water to move through it at lower temperatures (thereby reducing flooding of the catalyst layer and the cell in general); a key design strategy for water management. Water-flux measurements confirmed that better fuel-cell performance correlated to higher water removal through the anode. At higher temperatures, the cell performance does not correlate to the fractional anode water-removal rate, which decreased with increasing temperature. Thus, the improved GDL enables better water management at the moderate temperatures traversed or operated at under automotive conditions, but does not have a significant impact at high temperature where water exists and transports mainly in the vapor phase and very low temperatures where the cell is flooded. The *ex-situ* characterization studies of the GDLs revealed significant morphological differences between them, where serendipitous banded regions with high and low fiber densities were observed for the better performing GDL. This modulated structure resulted in high porosity regions where water preferentially flows and that are expected to impart high permeability for water removal and, more importantly, also resulted in easier droplet water removal into the channel from the GDL surface. Further studies are required to ascertain the optimal density modulations based on this materials strategy for the best fuel-cell performance for a wide range of operating conditions. The understanding gained can help fuel-cell material designers and component manufacturers, and provides new insights into fuel-cell water management, especially with ultra-thin catalyst layers.

4. Experimental Section

4.1. Materials fabrication and assembly

Catalyst-coated membranes (CCMs) were fabricated on pilot scale continuous production equipment with 0.05 $\mathrm{mg_{Pt}cm^{-2}}$ PtCoMn/NSTF anode electrodes, and 0.15 $\mathrm{mg_{Pt}cm^{-2}}$ PtCoMn/NSTF cathodes, and 20 µm thick 3M 825EW PEMs; details of NSTF electrode and CCM fabrication can be found elsewhere.[7] Experimental anode GDLs were prepared identically with either Mitsubishi Rayon Corporation (MRC) U105 or an experimental MRC backing, labeled “C”. As received backings were treated with a proprietary 3M hydrophobization process, then coated with nominally identical microporous layers containing carbon and hydrophobic agents. The cathode GDL in all cases was MRC U105 with the same finishing processes as used for the anode GDLs. While some intrinsic variability in MEAs is expected, the production processes used here have historically produced materials with reproducible performance properties, sand the data is consistent from replicate MEAs.

Hardstop Teflon-coated fiberglass gaskets were selected to provide 10 % compressive strain to the GDLs. A typical 50 cm^2 electrode area, quad-serpentine test cell obtained from Fuel Cell Technologies was used for the cell testing. All MEAs were first conditioned using a process referred to as "thermal cycling" and as described in [41]. (See Supplemental Experimental Procedures for further details on cells and materials).

4.2. Cell measurements

For each anode GDL type, three series of experiments were conducted to evaluate the performance sensitivity and water balance characteristics over a range of operating temperatures, current densities, and anode pressures, summarized in Table S1. For the temperature sensitivity test, MEA H_2/Air performance was evaluated as a function of cell temperature between 80 and 30°C. The cell current density was scanned from 0.02 Acm^{-2} up to an upper limit of 2.0 Acm^{-2} in a mixed linear/log-stepping mode with 120 s dwell time at each condition. Temperature sensitivity was determined from the 100 % RH curves by interpolating the cell current density achieved at 0.5 V cell voltage during the low-to-high current density sweep of the polarization curve. An additional reference polarization curve was measured at 80°C cell temperature with 68°C anode and cathode dewpoints, with all other conditions unchanged.

For the water balance tests, MEAs were evaluated at a series of operating temperatures, anode reactant pressures, and current densities and MEA product water was collected from the anode and cathode effluent streams (see Table S3 for quantification of the standard deviations).

4.3. Neutron imaging

High and low resolution neutron radiography was performed at the NIST Center for Neutron Research (NCNR) on thermal beam tube 2.[42,43] High-resolution radiography of through-plane water distribution was performed using an MCP detector with a pixel pitch of 5 μm and nominal resolution of 13 μm using a neutron fluence rate of 7.5 x 10^5 $cm^{-2}s^{-1}$ and a rectangular slit (10 mm x 1 mm). The imaging was performed on 2.5 cm^2 active area MEAs incorporated in specially designed cells.[44] GDL thickness along the neutron path was 1.2 cm, which can be used to convert water thickness into a saturation profile, although the interfaces will not be quantitative due to smoothing and other issues.[16] GDLs were compressed to 80% of their uncompressed thickness. Neutron images were taken with exposure time of 2 minutes. After the cell reached steady state for a given operating condition, 10 consecutive neutron images were averaged and processed to generate water profiles across the thickness of fuel-cell components (resulting in effective exposure time of 20 minutes). Profiles of water distribution across the thickness of the cell are averages across the cell area, including regions under both lands and channels over 11 passes of a single-serpentine channel. More details about the high-resolution neutron imaging, cell hardware, and image processing can be found elsewhere.[16] The MEAs were originally conditioned in standard 50 cm^2 cells (similar to the water balance measurements) and then removed and cut to fit the smaller 2.5 cm^2 cells. Teflon gaskets were used around the 2.5 cm^2 GDLs in order to minimize neutron attenuation by the gaskets. Fuel-cell polarization curves and impedance spectra were obtained during imaging using a fuel-cell test stand (MicroE systems) and Zahner potentiostat, respectively. The cells were operated at fixed flows of 100 sccm at the anode and 200 sccm at the cathode with fully saturated inlet gases (H_2 and Air respectively). (See Supplemental Experimental Procedures for further details).

4.4. Transport property measurements

Thermal conductivity was measured using a custom-built apparatus, where a “constant heat flux” method was chosen.[45] A photograph of the setup and an equivalent resistor network to calculate GDL thermal resistances are provided in SI, Figure S8. Circular GDL samples of diameter 2.54 cm were positioned between the copper plates (for isothermal regions adjacent to GDLs) and 12L14 carbon steel rods of known thermal conductivity (54.9 $Wm^{-1}K^{-1}$ at 20°C, McMaster-Carr). Compression of the samples was monitored by placing this assembly onto Instron 5944 testing device. (See Supplemental Experimental Procedures for further details).

The effective diffusivity measurement setup and data analysis were reported previously.[46,47] Here salient details and modifications to the reported setup are presented. The method consists of measuring limiting current in an electrochemical hydrogen-pump experiment. The cell’s MEA included NR212 membrane with Pt/C catalyst loading of 0.4 $mgPtcm^{-2}$. On the counter/reference electrode dry SGL 10AA GDL was used, whereas on the working electrode dry or partially-saturated MRC GDLs were used. Limiting current was measured at 0.3 V, this potential was in the plateau region on the cyclic voltammetry curve, indicating double-layer charging region. Effective diffusion coefficient was computed with known limiting current, i_{lim}, thickness of the GDL, L_{GDL} and concentration of hydrogen:

$$D = \frac{i_{\lim} L_{GDL}}{2Fc_{H2O}} \quad [1]$$

Water-retention curves were measured using the setup described in [48,49]. In this method, the GDL is sandwiched between the hydrophilic and hydrophobic layers. The hydrophobic side is exposed to gas feed controlled by pressure transducer, whereas the hydrophilic layer is in contact with liquid feed connected to water reservoir, where mass of water is recorded to determine the amount of water entering the GDL sample. A syringe pump is used to control the injection/withdrawal rate and a pressure transducer records the pressure. The pressure range is varied between –30 and 30 kPa with a typical runtime of 8 hours.

Detachment velocity and adhesion-force measurements were performed on a rotating-stage goniometer (Rame-Hart) with a customized injection system. The detailed drawing of the set-up and a photograph can be found in [24,26]. (See Supplemental Experimental Procedures for further details).

4.5. Structural-property measurements

X-ray computed tomography for the GDL characterization was conducted at Beamline 8.3.2 at the Advanced Light Source (ALS). The source energy was set at 14 keV, resulting in intensity flux count of 8,000 for 300 ms exposure time.[40,50] (See Supplemental Experimental Procedures for further details). Optical imaging was done using a Nikon SMZ-1500 stereo microscope with a 1.6 plan objective. Images were acquired using a Nikon D1X digital SLR. Light sources used were the backlight of the diascopic stand as well as reflected light from a fiber optic illuminator. For stress-strain curves, the thickness of uncompressed GDLs was measured with a Mitutoyo Thickness Gage (Series 547, compressive force of 1.5 N equivalent to 0.04 MPa). Stress/strain was determined using a mechanical testing system (Instron 5944). Compression rate of the instrument was set at 25 μm min^{-1}.

Supporting Information

Supplemental Information includes Supplemental Experimental Procedures, 18 figures, 3 tables, and can be found with this article online

Author Contributions

D.S.H, A.K1, A.K2, J.M., M.J.P., M.R., A.D.S., J.M.S., D.S., I.V.Z, and A.Z.W. designed and performed experiments, A.J.S., D.S.H., I.V.Z and A.Z.W. analyzed the data and wrote the paper. I.V.Z and A.Z.W. finalized the final draft. R.B., R.M., J.S.A., and A.Z.W. provided supervision and feedback.

Acknowledgements

We would like to acknowledge the US Department of Energy, which provided funding for this work under contract DE-AC02-05CH11231. This work was supported by the Office of Fuel Cell Technologies at the U.S. Department of Energy-Energy Efficiency and Renewable Energy. The authors would like to thank Technology Development Managers Nancy Garland and Dimitrios Papageorgopoulos for supporting this work. This work was also supported by the U.S. Department of Commerce, the NIST Ionizing Radiation Division, the Director's Office of NIST, the NIST Center for Neutron Research, and the Department of Energy through interagency agreement no. DE-AI01-01EE50660. The Advanced Light Source is supported by the Director, Office of Science, Office of Basic Energy Sciences, of the U.S. Department of Energy under Contract No. DE-AC02-05CH11231.

References

1. Galbiati, S., Morin, A., and Pauc, N. (2014). Supportless Platinum Nanotubes Array by Atomic Layer Deposition as PEM Fuel Cell Electrode. Electrochim Acta *125*, 107-116.
2. Shukla, S., Domican, K., Karan, K., Bhattacharjee, S., and Secanell, M. (2015). Analysis of Low Platinum Loading Thin Polymer Electrolyte Fuel Cell Electrodes Prepared by Inkjet Printing. Electrochim Acta *156*, 289-300.
3. Inaba, M., Suzuki, T., Hatanaka, T., and Morimoto, Y. (2015). Fabrication and Cell Analysis of a Pt/SiO2 Platinum Thin Film Electrode. Journal of The Electrochemical Society *162*, F634-F638.
4. Tian, Z.Q., Lim, S.H., Poh, C.K., Tang, Z., Xia, Z., Luo, Z., Shen, P.K., Chua, D., Feng, Y.P., Shen, Z., *et al.* (2011). A Highly Order-Structured Membrane Electrode Assembly with Vertically Aligned Carbon Nanotubes for Ultra-Low Pt Loading PEM Fuel Cells. Advanced Energy Materials *1*, 1205-1214.
5. Zhang, W., Minett, A.I., Gao, M., Zhao, J., Razal, J.M., Wallace, G.G., Romeo, T., and Chen, J. (2011). Integrated High-Efficiency Pt/Carbon Nanotube Arrays for PEM Fuel Cells. Advanced Energy Materials *1*, 671-677.
6. Fujigaya, T., and Nakashima, N. (2013). Fuel Cell Electrocatalyst Using Polybenzimidazole-Modified Carbon Nanotubes As Support Materials. Advanced Materials *25*, 1666-1681.
7. Debe, M.K., Hester, A.E., Vernstrom, G.D., Steinbach, A.J., Hendricks, S.M., Schmoeckel, A.K., Atanasoski, R.T., McClure, D.J., Turner, P.L. (2007). Nanostructured Thin Film Catalysts for PEM Fuel Cells by Vacuum Web Coating. Paper presented at: 50th Annual Technical Conference of the Society of Vaccum Coaters (Louisville, KY).
8. Debe, M.K., Schmoeckel, A.K., Vernstrom, G.D., and Atanasoski, R. (2006). High voltage stability of nanostructured thin film catalysts for PEM fuel cells. Journal of Power Sources *161*, 1002-1011.
9. Sinha, P.K., Gu, W., Kongkanand, A., and Thompson, E. (2011). Performance of Nano Structured Thin Film (NSTF) Electrodes under Partially-Humidified Conditions. Journal of The Electrochemical Society *158*, B831-B840.
10. Debe, M.K. (2012). Electrocatalyst approaches and challenges for automotive fuel cells. Nature *486*, 43-51.
11. Zenyuk, I.V., Das, P.K., and Weber, A.Z. (2016). Understanding Impacts of Catalyst-Layer Thickness on Fuel-Cell Performance via Mathematical Modeling. Journal of The Electrochemical Society *163*, F691-F703.
12. Zenyuk, I.V., and Litster, S. (2014). Modeling ion conduction and electrochemical reactions in water films on thin-film metal electrodes with application to low temperature fuel cells. Electrochim Acta *146*, 194-206.
13. Steinbach, A.J., Debe, M.K., Pejsa, M.J., Peppin, D.M., Haug, A.T., Kurkowski, M.J., and Maier-Hendricks, S.M. (2011). Influence of Anode GDL on PEMFC Ultra-Thin Electrode Water Management at Low Temperatures. ECS Transactions *41*, 449-457.
14. Steinbach, A.J., Debe, M.K., Wong, J., Kurkowski, M.J., Haug, A.T., Peppin, D.M., Deppe, S.K., Hendricks, S.M., and Fischer, E.M. (2010). A New Paradigm for PEMFC Ultra-Thin Electrode Water Management at Low Temperatures. ECS Transactions *33*, 1179-1188.
15. Steinbach, A.J., Debe, M.K., and Haug, A.T. (2016). Fuel cell water management via reduced anode reactant pressure (US Patent 9,276,273).

16. Fairweather, J.D., Spernjak, D., Weber, A.Z., Harvey, D., Wessel, S., Hussey, D.S., Jacobson, D.L., Artyushkova, K., Mukundan, R., and Borup, R.L. (2013). Effects of Cathode Corrosion on Through-Plane Water Transport in Proton Exchange Membrane Fuel Cells. Journal of The Electrochemical Society *160*, F980-F993.
17. Weber, A.Z., and Newman, J. (2006). Coupled thermal and water management in polymer electrolyte fuel cells. Journal of the Electrochemical Society *153*, A2205-A2214.
18. Kim, S., and Mench, M.M. (2009). Investigation of temperature-driven water transport in polymer electrolyte fuel cell: Phase-Change-Induced Flow. Journal of the Electrochemical Society *156*, B353-B362.
19. Zhou, J., Stanier, D., Putz, A., and Secanell, M. (2017). A Mixed Wettability Pore Size Distribution Based Mathematical Model for Analyzing Two-Phase Flow in Porous Electrodes II. Model Validation and Analysis of Micro-Structural Parameters. Journal of the Electrochemical Society *164*, F540-F556.
20. Hickner, M.A., Siegel, N.P., Chen, K.S., Hussey, D.S., Jacobson, D.L., and Arif, M. (2008). In Situ High-Resolution Neutron Radiography of Cross-Sectional Liquid Water Profiles in Proton Exchange Membrane Fuel Cells. Journal of The Electrochemical Society *155*, B427-B434.
21. Weber, A.Z., and Hickner, M.A. (2008). Modeling and high-resolution-imaging studies of water-content profiles in a polymer-electrolyte-fuel-cell membrane-electrode assembly. Electrochim Acta *53*, 7668-7674.
22. Zenyuk, I.V., Lamibrac, A., Eller, J.J., Parkinson, D.Y., Marone, F., Büchi, F.N., and Weber, A.Z. (2016). Investigating Evaporation in Gas Diffusion Layers for Fuel Cells with X-ray Computed Tomography. The Journal of Physical Chemistry C.
23. Zhou, J., Putz, A., and Secanell, M. (2017). A Mixed Wettability Pore Size Distribution Based Mathematical Model for Analyzing Two-Phase Flow in Porous Electrodes I. Mathematical Model. Journal of the Electrochemical Society *164*, F530-F539.
24. Santamaria, A.D., Das, P.K., MacDonald, J.C., and Weber, A.Z. (2014). Liquid-Water Interactions with Gas-Diffusion-Layer Surfaces. Journal of The Electrochemical Society *161*, F1184-F1193.
25. Quesnel, C., Cao, R., Lehr, J., Kietzig, A.M., Weber, A.Z., and Gostick, J.T. (2015). Dynamic Percolation and Droplet Growth Behavior in Porous Electrodes of Polymer Electrolyte Fuel Cells. J Phys Chem C *119*, 22934-22944.
26. Das, P.K., Grippin, A., Kwong, A., and Weber, A.Z. (2012). Liquid-water-droplet adhesion-force measurements on fresh and aged fuel-cell gas-diffusion layers. Journal of The Electrochemical Society *159*, B489-B496.
27. Forner-Cuenca, A., Biesdorf, J., Gubler, L., Kristiansen, P.M., Schmidt, T.J., and Boillat, P. (2015). Engineered Water Highways in Fuel Cells: Radiation Grafting of Gas Diffusion Layers. Advanced Materials *27*, 6317-6322.
28. Alink, R., Haussmann, J., Markotter, H., Schwager, M., Manke, I., and Gerteisen, D. (2013). The influence of porous transport layer modifications on the water management in polymer electrolyte membrane fuel cells. Journal of Power Sources *233*, 358-368.
29. Gerteisen, D., Heilmann, T., and Ziegler, C. (2008). Enhancing liquid water transport by laser perforation of a GDL in a PEM fuel cell. Journal of Power Sources *177*, 348-354.
30. Gerteisen, D., and Sadeler, C. (2010). Stability and performance improvement of a polymer electrolyte membrane fuel cell stack by laser perforation of gas diffusion layers. Journal of Power Sources *195*, 5252-5257.

31. Haußmann, J., Markötter, H., Alink, R., Bauder, A., Dittmann, K., Manke, I., and Scholta, J. (2013). Synchrotron radiography and tomography of water transport in perforated gas diffusion media. Journal of Power Sources *239*, 611-622.
32. Lu, Z., Waldecker, J., Xie, X., Lai, M.-C., Hussey, D.S., and Jacobson, D.L. (2013). Investigation of Water Transport in Perforated Gas Diffusion Layer by Neutron Radiography. ECS Transactions *58*, 315-324.
33. Manahan, M., Hatzell, M., Kumbur, E., and Mench, M. (2011). Laser perforated fuel cell diffusion media. Part I: Related changes in performance and water content. Journal of Power Sources *196*, 5573-5582.
34. Manahan, M.P., and Mench, M.M. (2012). Laser Perforated Fuel Cell Diffusion Media: Engineered Interfaces for Improved Ionic and Oxygen Transport. Journal of the Electrochemical Society *159*, F322-F330.
35. Markotter, H., Alink, R., Haussmann, J., Dittmann, K., Arlt, T., Wieder, F., Totzke, C., Klages, M., Reiter, C., Riesemeier, H., *et al.* (2012). Visualization of the water distribution in perforated gas diffusion layers by means of synchrotron X-ray radiography. Int J Hydrog Energy *37*, 7757-7761.
36. Markotter, H., Haussmann, J., Alink, R., Totzke, C., Arlt, T., Klages, M., Riesemeier, H., Scholta, J., Gerteisen, D., Banhart, J., *et al.* (2013). Influence of cracks in the microporous layer on the water distribution in a PEM fuel cell investigated by synchrotron radiography. Electrochem Commun *34*, 22-24.
37. Nishida, K., Murakami, T., Tsushima, S., and Hirai, S. (2010). Measurement of liquid water content in cathode gas diffusion electrode of polymer electrolyte fuel cell. Journal of Power Sources *195*, 3365-3373.
38. Zenyuk, I.V., Taspinar, R., Kalidindi, A.R., Kumbur, E.C., and Litster, S. (2014). Computational and Experimental Analysis of Water Transport at Component Interfaces in Polymer Electrolyte Fuel Cells. Journal of The Electrochemical Society *161*, F3091-F3103.
39. Owejan, J.P., Owejan, J.E., Gu, W.B., Trabold, T.A., Tighe, T.W., and Mathias, M.F. (2010). Water Transport Mechanisms in PEMFC Gas Diffusion Layers. Journal of the Electrochemical Society *157*, B1456-B1464.
40. Zenyuk, I.V., Parkinson, D.Y., Hwang, G., and Weber, A.Z. (2015). Probing water distribution in compressed fuel-cell gas-diffusion layers using X-ray computed tomography. Electrochem Commun *53*, 24-28.
41. Ahluwalia, R.K., Peng, J.-K., Wang, X., Cullen, D.A., and Steinbach, A.J. (2017). Long-Term Stability of Nanostructured Thin Film Electrodes at Operating Potentials. Journal of The Electrochemical Society *164*, F306-F320.
42. Hussey, D.S., Spernjak, D., Weber, A.Z., Mukundan, R., Fairweather, J., Brosha, E.L., Davey, J., Spendelow, J.S., Jacobson, D.L., and Borup, R.L. (2012). Accurate measurement of the through-plane water content of proton-exchange membranes using neutron radiography. Journal of Applied Physics *112*, 104906.
43. Mukundan, R., and Borup, R.L. (2009). Visualising Liquid Water in PEM Fuel Cells Using Neutron Imaging. Fuel Cells *9*, 499-505.
44. Mukundan, R., Davey, J.R., Rockward, T., Spendelow, J.S., Pivovar, B., Hussey, D.S., Jacobson, D.L., Arif, M., and Borup, R. (2007). Imaging of Water Profiles in PEM Fuel Cells Using Neutron Radiography: Effect of Operating Conditions and GDL Composition. ECS Transactions *11*, 411-422.

45. Burheim, O., Vie, P.J.S., Pharoah, J.G., and Kjelstrup, S. (2010). Ex situ measurements of through-plane thermal conductivities in a polymer electrolyte fuel cell. Journal of Power Sources *195*, 249-256.
46. Hwang, G.S., and Weber, A.Z. (2012). Effective-Diffusivity Measurement of Partially-Saturated Fuel-Cell Gas-Diffusion Layers. Journal of the Electrochemical Society *159*, F683-F692.
47. Spingler, F.B., Phillips, A., Schuler, T., Tucker, M.C., and Weber, A.Z. (2017). Investigating Fuel-Cell Transport Limitations using Hydrogen Limiting Current. Int J Hydrog Energy, doi: 10.1016/j.ijhydene.2017.1001.1036.
48. Gostick, J.T., Fowler, M.W., Ioannidis, M.A., Pritzker, M.D., Volfkovich, Y.M., and Sakars, A. (2006). Capillary pressure and hydrophilic porosity in gas diffusion layers for polymer electrolyte fuel cells. Journal of Power Sources *156*, 375-387.
49. Gunterman, H.P.F. (2011). Characterization of Fuel-Cell Diffusion Media.
50. Groso, A., Abela, R., and Stampanoni, M. (2006). Implementation of a fast method for high resolutionphase contrast tomography. Opt Express *14*, 8103-8110.
51. Zenyuk, I.V., Parkinson, D.Y., Connolly, L.G., and Weber, A.Z. (2016). Gas-diffusion-layer structural properties under compression via X-ray tomography. Journal of Power Sources *328*, 364-376.

Graphical Abstract

Novel anode porous-electrode material for fuel-cell applications with increased ability to permeate water and enable operation of ultra-thin catalyst layers for high-power-density performance at low temperatures. Water profile is shown on the left, schematic of fuel cell processes in the middle and performance curve on the bottom right.

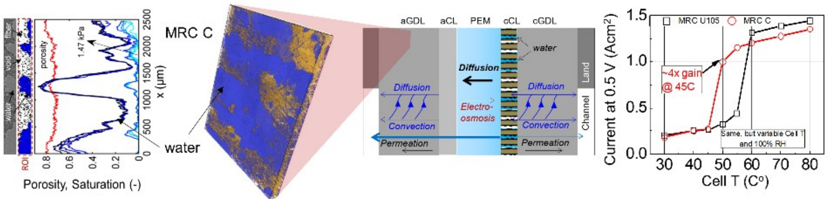

Supporting Information

Anode-design strategies for improved performance of polymer-electrolyte fuel cells with ultra-thin electrodes

A. J. Steinbach[a], J. S. Allen[g], R. Borup[b], D. S. Hussey[c], D. L. Jacobson[c], A. Komlev[a], A. Kwong,[d] J. MacDonald[d], R. Mukundan[b], M. J. Pejsa[a], M. Roos[d], A. D. Santamaria[d,f], J. M. Sieracki[a], D. Spernjak[b], I. V. Zenyuk[d,e] and A. Z. Weber[d]*

[a] 3M Company, Fuel Cell Components Program, 3M Center, St. Paul, MN 55144, USA
[b] Los Alamos National Laboratory, MS D429, MPA-11, Los Alamos, NM 87545
[c] NIST Center for Neutron Research, 100 Bureau Drive, MS 8461, Gaithersburg, MD 20899
[d] Lawrence Berkeley National Laboratory, 1 Cyclotron Rd, MS70-108B Berkeley, CA 94720
[e] Mechanical Engineering Department, Tufts University, 200 Boston Ave. 2600, Medford, MA 02155
[f] Mechanical Engineering Department, Western New England University, 1215 Wilbraham Road, Springfield, MA 01119
[g] Department of Mechanical Engineering – Engineering Mechanics, Michigan Technological University, 1400 Townsend Drive Houghton, MI 49931

(*) to whom correspondence should be addressed. E-mail: azweber@lbl.gov

The outline of the Supporting Information is the following:

1. Experimental Procedure and schematic of phenomena
2. Cell performance and water-balance results
3. Neutron imaging data at various current densities and for low-resolution imaging.
4. Complementary results on *ex-situ* characterization.
5. Results from alternate GDL

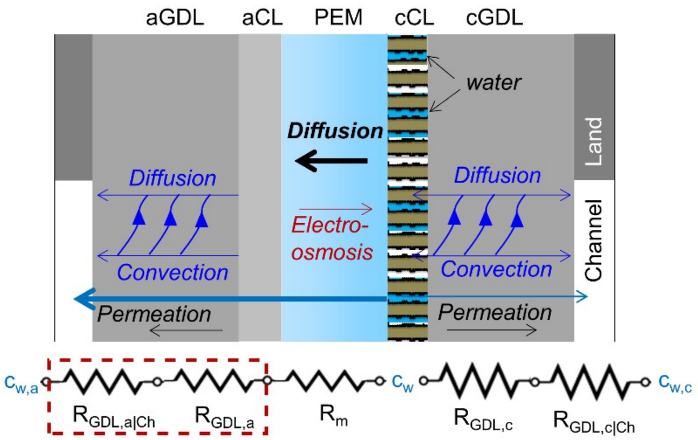

Figure S1. Schematic of PEFC water-transport processes with a NSTF cathode operating at high RH, where resistances for water removal going from cathode catalyst layer (cCL) to cathode GDL (cGDL) or through the membrane (m) to anode CL (aCL) and GDL (aGDL) are shown.

Cell Measurements

Cell measurements were conducted in 50 cm^2 test cells with quad serpentine flow fields with land and channel widths of ca. 0.8 mm, obtained from Fuel Cell Technlogies, Inc. MEAs consisted of 3M NSTF catalyst coated membranes, 3M 2979 cathode GDLs, and the stated anode GDL. The catalyst coated membranes contained PtCoMn/NSTF anode and cathode catalysts with 0.05 and 0.15 mg cm^{-2} areal Pt loadings in the electrods and a 20 µm thick, 3M 825EW PFSA membrane. The anode and cathode diffusion media were compressed to approximately 10% average strain.

Table S1 List of operating conditions for temperature sensitivity MEA evaluation and MEA product water-balance series.

Series	Cell T [°C]	Current density [Acm^{-2}]	Anode Stoich. [H_2]	Anode Pressure [kPag]	Anode RH [%]	Cathode Stoich [Air]	Cath. Pressure [kPag]	Cath. RH [%]
Temp. Sensitivity	80 to 30	0.02→ 2	2	50	100	2.5	50	100
Water balance: Temp.	60 to 30	0.25 to 1.5 0.25→1.5	2	0	0	2	0	0
Water balance: anode pressure	65, 50, 40	0.25→1.5	2	0, 50, 100	0	2	50	0

Table S1 lists the operating condition matrix for these measurements. In the temperature sensitivity series, the temperature difference between each measurement was 5°C. The minimum allowed voltage in the polarization curve was 0.4 V, and the current step size was 0.25 $\mathrm{Acm^{-2}}$ for both series. Product water collections were made with a custom-built, automated water collection system. The cell effluent streams were passed through individual tube-in-tube heat exchangers to substantially condense out water vapor, and then liquid product water was collected in chilled, insulated separatory funnels and the gas-phase effluent streams were vented. The heat exchangers and separatory funnels were chilled to 5°C. After sufficient operating time (> 30 minute), computer-controlled solenoid valves were periodically opened to allow the collected liquid water to drain to computer-interfaced balances, where the initial and final masses were recorded. Three measurements were made in succession at each operating condition. Anode and cathode liquid effluent water flow rates were corrected for the assumed residual 5°C dewpoint vapor in the vented effluent streams and the collection efficiency (typically > 90%).

Low-Resolution Neutron Imaging

Low-resolution radiography of in-plane water distribution across a 50 $\mathrm{cm^2}$ cell was performed using an amorphous-Si detector with a pixel pitch of 127 µm and a nominal resolution of 300 µm using a neutron fluence rate of 1.4 x 10^7 $\mathrm{cm^{-2}s^{-1}}$ and circular slit (15 mm). Images were taken with exposure time of 10 seconds, where the water distribution at steady-state cell operation was obtained by averaging 60 consecutive images (resulting in effective exposure time of 10 minutes). The imaging was performed on 50 $\mathrm{cm^2}$ active area MEAs incorporated in specially designed fuel-cell hardware using standard quad-serpentine flow fields. Fuel-cell polarization curves and impedance spectra were obtained during imaging using a fuel-cell test stand (MicroE systems) and Zahner potentiostat, respectively.

Transport-property measurements

Thermal-conductivty measurements: The main body of the experimental set-up is thermally insulated by a porous polyurethane insulation with a soft ceramic tape lining. A temperature gradient of 20°C across the setup was applied with water/aluminum heat exchangers. Thermally conductive grease was used to minimize thermal resistance at the metal-to-metal contacts. Eight thin, PFA-insulated thermocouples (Omega TC-TT-T-36-36) were used to measure temperature at the radial depth of 1 cm and at different locations within the steel rods. Thermal conductivity of the GDLs was separated from thermal contact resistance by performing the experiment on various numbers of stacked GDL samples.

Detachment-velocity measurements: 3 x 3 cm GDL samples were placed onto the injection port. The pressure of the injecting system was measured by an Omega PX603 pressure transducer. To simulate parallel air flow over the sample, a Lexan flow channel (4 x 7 mm) was placed over the formed droplet. Dry air flowrate at 20°C was controlled by Omega FMA-2609A flow controller (with maximum flow rate of 50 $\mathrm{Lmin^{-1}}$). The droplet was considered to be detached when its position was outside of its wetting area, and the detachment velocity was defined as the average channel flow at this point.

Structural-property measurements

X-ray Computed Tomography: An optics system consisted of sCMOS PCO.Edge camera with 3.3 x 3.3 mm field of view (FOV), a 0.5 mm LuAG scintillator and 5x lenses, resulting in an image with a 1.33 µm pixel resolution. 1025 projections were acquired for each tomographic scan during 180° rotation. Image reconstruction of the acquired back-projection images was performed with Modified Bronnikov Algorithm (MBA), which is incorporated into commercial software Fiji and Octopus 8.5 [44]. Smoothing filter was applied to remove ring artifacts. Fiji was used for preliminary raw image data transformation and cropping to a FOV of 2.5 x 2.5 mm. The sample holder used for X-ray CT imaging consists of an aluminum stage, and a high X-ray transmitting Vespel® cup. A 3.2 mm diameter GDL sample is pressed against the aluminum stage with a flat stamp. Two types of experiments were conducted: 1) compression study and 2) water-injection study. For the compression study, the GDL was compressed with a flat stamp and imaged with the level of compression determined by measuring its thickness via imaging. For the second experiment, liquid pressures were set with a static liquid-water column connected to the sample stage for a steady-state experiment. First, a dry GDL was imaged and then liquid pressure was applied in increments. The experiments were stopped when liquid-pressure breakthrough was reached. The schematic of the sample holder and all the details for image processing and analysis has been reported previously.[45]

Results

Cell Voltage at Current Density of 0.25 A/cm2 for Various Temperatures

Figure S2 shows cell voltage plots for MRC U105 and MRC C at constant current density of 0.25 A/cm^2. As shown in Figure S2a, the cell voltage decreases with decreasing temperature for both GDL types, but the performance of the MEA with MRC C decreases more slowly. Furthermore, liquid water anode removal rates are larger for lower temperatures and also larger for MRC C, as shown by Figure S2b. With decreasing temperature, the amount of total water removed via anode saturates for MRC C at a value of 0.8 µL/cm^2/min and for MRC U105 at the value of 0.5 µL/cm^2/min, as shown by Figure S2c. As the water effluent rate out the anode increases at fixed operating conditions, the water effluent rate out the cathode decreases commensurately. Since the testing here was conducted with dry inlet gases, it is reasonable that a portion of the product water which exits the cell cathode is in the vapor phase with the balance in the liquid phase. For each cell temperature, the maximum vapor phase water removal rate out of the cell cathode was calculated, based on the assumption of 100% saturation at the cathode exit gas conditions (flow rate, pressure, and temperature). The liquid water removal rate was then calculated by subtracting the calculated vapor phase water removal rate from the measured cathode water removal rate, and is plotted in Figure S2d. This calculation indicates that at most cell temperatures, there is a lower overall tendency for liquid water transport out the cathode GDL for the MEA with the MRC "C" anode GDL than with the U105 anode.

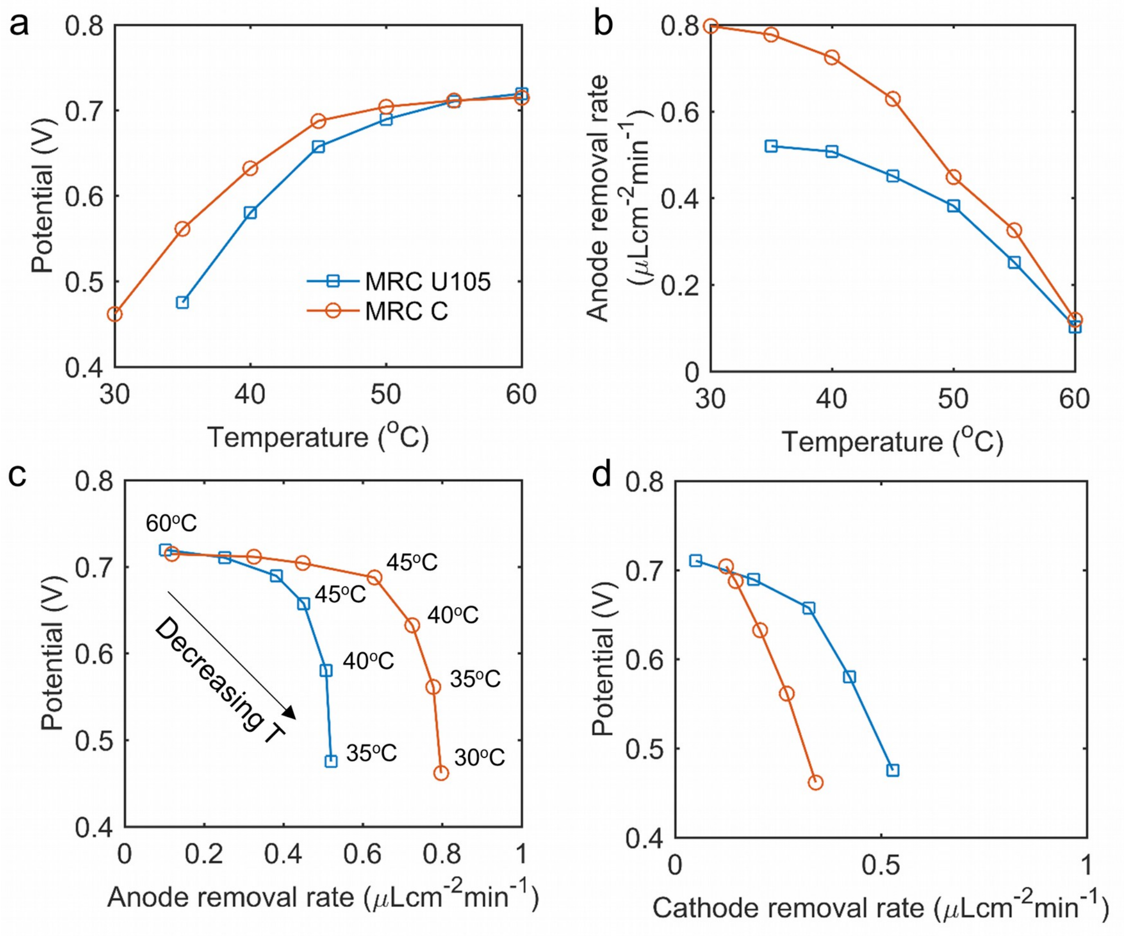

Figure S2 a) Cell voltage at 0.25 A/cm^2, and b) product water distribution sensitivity to temperature. c) Performance sensitivity to total anode water removal rate and d) cathode liquid removal rate.

Product Water Balance Pressure Series

It should be noted that the results obtained are reproducible and generally consistent among different GDL types. Figure S3 summarizes results from a series that evaluated the influence of anode operating pressure and cell temperature on performance and product water balance for the MEAs with either anode GDL (Table S1, third row). Polarization curves measured with both anode GDLs revealed similar trends, in that performance improved monotonically as cell temperature increased from 40 °C to 65°C at a given anode pressure. At 40 and 50°C, performance decreased monotonically as anode pressure was increased from 1 bar to 2 bar, whereas at 65°C performance was relatively insensitive. At 40 and 50°C, higher performance was obtained with the MEA with MRC C anode GDL than with the MRC U105 anode GDL. The product water distributions were also sensitive to pressure and operating temperature. As the anode pressure increased, the fraction of product water removed via the anode decreased. The largest fraction of product water removed at a given anode pressure occurred at 50°C with both anode GDLs.

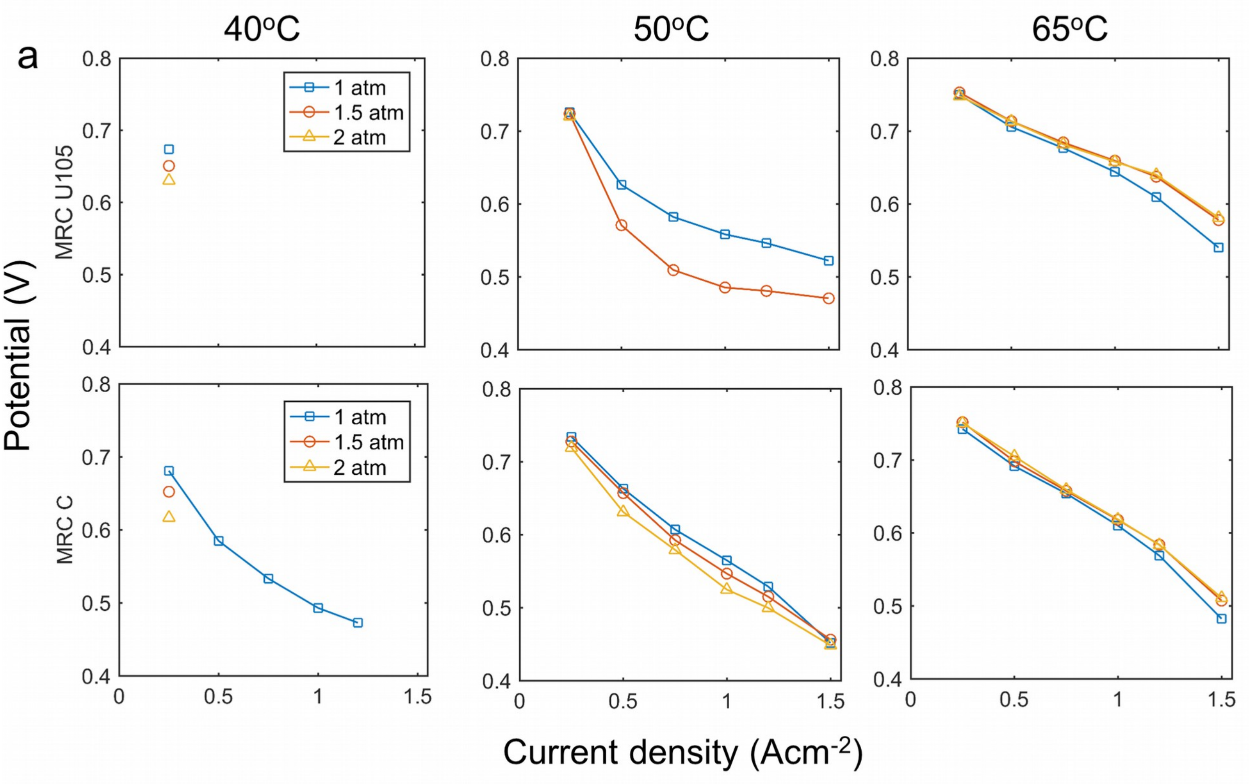

Figure S3 Measured cell voltage and fraction of product water removed out anode from anode pressure series at 50 °C cell temperature, 1.52 kPa air, constant stoichiometry 2/2, and dry inlet gases.

Figure S4 summarizes the calculated product water flow rate exiting the cathode in the liquid phase, based on the data shown in Figure S3 and using the calculation method described for Figure S2d, above . For reference, the water generation rate is 5.58 µL cm^{-2} min^{-1}. At 40 °C, all cathode liquid water flow rates were below 1 µL cm^{-2} min^{-1} due to the relatively high anode removal rates shown above. At 0.25 A/cm^{2}, the liquid water removal rates were modestly lower at a given pressure with MRC C than with U105. At 50°C, cathode liquid water flow rates increased with increasing anode pressure and increasing current density. At 1.5atm anode pressure, both the MRC C and MRC U105 were able to operate up to 1.5 A/cm^{2} current densities, allowing direct comparison of the influence of anode GDL type. At all current densities between 0.25 and 1.5 A cm^{-2}, the liquid water removal rate was lower with MRC C than U105. At 65°C, no liquid water removal out the cathode was calculated to occur at 1 and 1.5 atm anode pressures, but substantial liquid water removal rates were calculated to occur with 2 atm anode pressure. At 65°C, little difference in water liquid water removal rates between MRC C and U105 was observed, in contrast to the observations at lower temperatures. One possible reason for this discrepancy may be that as the temperature increases, the extent of vapor phase cathode water removal through the GDL may be higher than predicted in the simple model above, due to a temperature gradient across the cathode GDL.

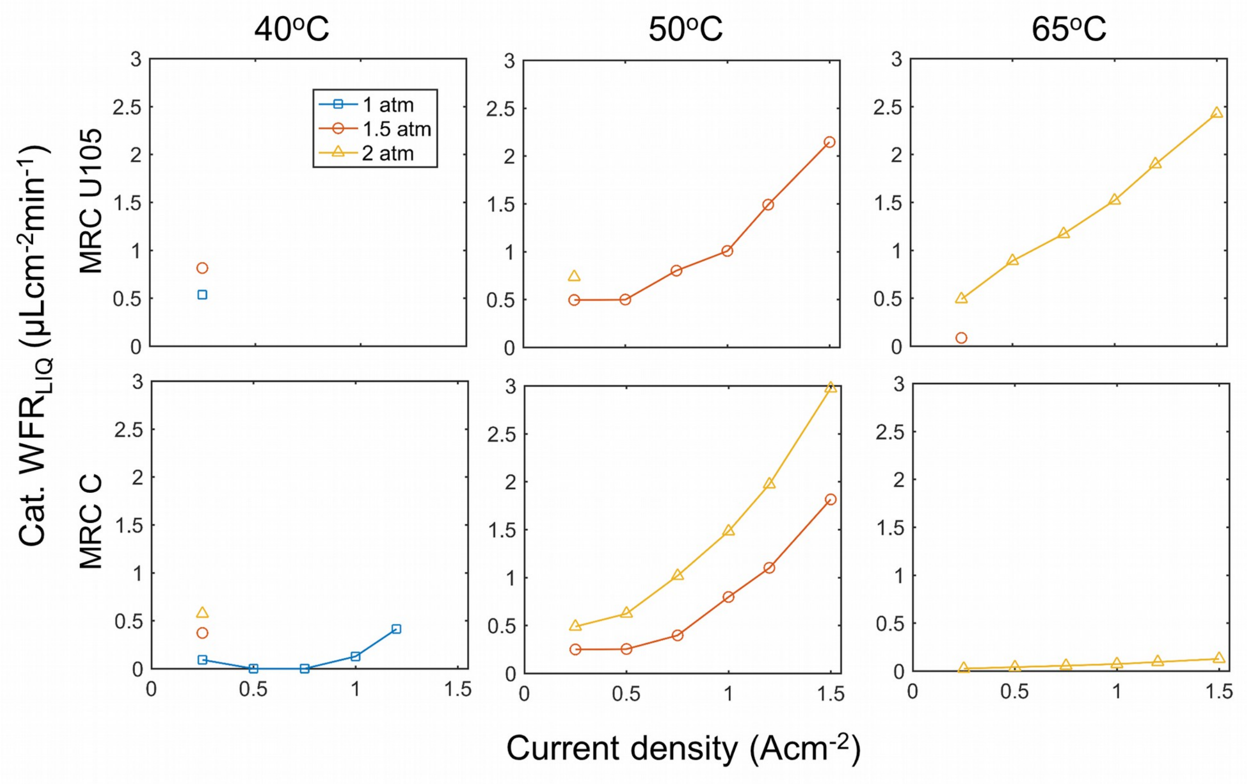

Figure S4 Calculated liquid water flow rates exiting cathode for a range of currents, temperatures and anode pressure (PA).

Each water effluent measurement point (at a specific temperature, pressure, and current density) is the average value from 3 consecutive measurement trials. The standard deviation of the three trials was calculated. Table S3 summarizes the median relative standard deviation of the water for both the anode and cathode collection devices as a function of collected flowrate. The relative standard deviation between 0 to 0.5 μL cm^{-2} min^{-1} was 17.9%, and decreased to 10.8% or less as the flowrate increased. The overall average collection efficiency of the device (anode and cathode combined) was calculated to be 95 ± 4.0 % over all measurements.

Table S2. Water-balance-data error quantification.

Effluent Flow Rate (μL cm^{-2} min^{-1}	Median anode relative standard deviation (%)	Median cathode relative standard deviation (%)
0-0.5	17.9	NA
0.5-1	10.8	6.7
1.0-2.0	5.1	4.8
2.0-3.7	3.8	2.7
3.7-7.0	NA	2.6

Neutron Imaging Studies

The water profiles of the cell operated at 80°C at open circuit voltage (OCV) and current densities of 0.4, 0.8 and 1.2 A/cm2 for MRC 105 and MRC are reported in Figures S4a and b. For all current densities the levels of liquid water in the anode are higher for MRC U105 compared to MRC C. However, the overall water thicknesses even for the highest current density of 1.2 A/cm^2 are fraction of those at 40°C (see Figure S4). The peak in water thickness for all the current densities at 80°C is observed near the membrane, indicating that GDLs remain relatively free of saturated water. The MEA water content at the highest current density (1.2 A/cm^2) is actually slightly lower than the water content at 0.8 A/cm^2 due to more heat generation at the highest current density. This result is consistent with previously reported low-resolution neutron imaging results. There is also a significant increase in the anode GDL water saturation with increasing current density. For example, the anode GDL water saturation calculated from the flat portion of the profile within the anode GDL substrate increases by an order of magnitude (from 0.5 % to 5 % liquid water saturation) when the current is increased from 0.4 A/cm^2 to 0.8 A/cm^2. The anode GDL water saturation is also 2 to 3 times the cathode GDL water saturation indicating the importance of water removal through the anode in controlling the MEA water content. The water profiles in the cell using the MRC C anode GDL is illustrated in Figure S5b and shows slightly lower water content under all the measured conditions. The anode GDL water saturation does not increase in this cell as dramatically as the cell with the MRC U105 GDL. For example, the anode GDL water saturation of the MRC C GDL is 5 times lower (30 % lower) than the MRC U105 GDL at 0.8 A/cm^2 (1.2 A/cm^2). This decreased anode GDL water saturation also results in lower MEA water content under all the conditions measured.

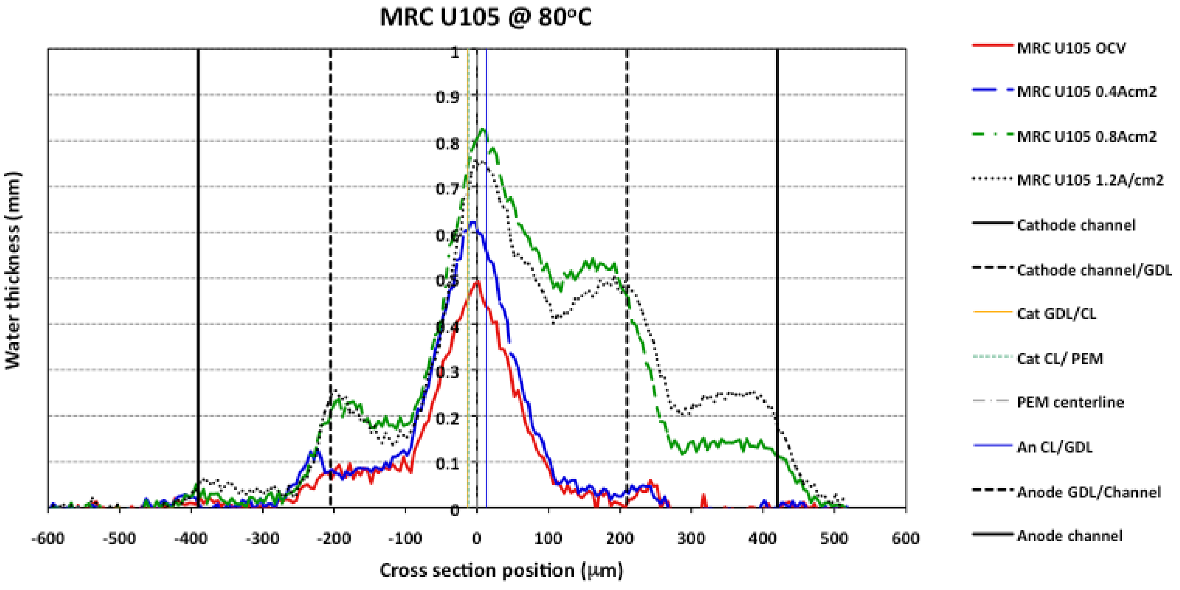

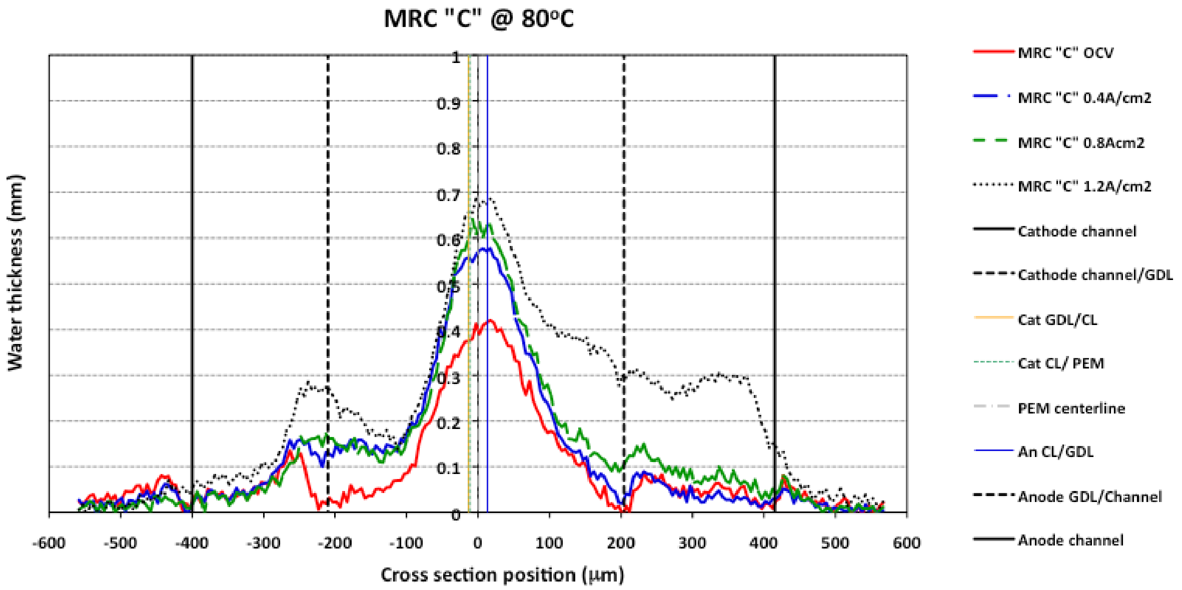

Figure S5 Water profiles of the PEFCs with a) MRC U105 and b) MRC C cathode GDLs operated at 80°C at various current densities. Cathode locations correspond to cross-section positions less than zero.

The water profiles of the cell with the MRC U105 anode GDL operated at 40 °C at open circuit voltage (OCV), 0.3 V and 0.1 V is reported in Figure S6a. In addition to the MEA water content increasing with decreasing operating voltage (increasing current density), water peaks within both the cathode and anode GDLs appear at the lower voltages. The anode GDL water saturation is also significantly higher (up to a value of 30%) than the cathode GDL water saturation indicating that the anode GDL plays a critical role in water removal. The cathode GDL water content peaks at intermediate current densities indicating a balance between heat generated and water produced at the cathode. However, the anode GDL water saturation does not decrease even at a potential of 0.1 V, suggesting that a significant fraction of the heat is removed from the cathode side while a significant fraction of the water is removed from the anode side (twice the amount of liquid water on the anode channels when compared to the cathode channels). The water profiles of the cell with the MRC C anode GDL under identical conditions are illustrated in Figure S6b. The water content in this cell is significantly lower at all locations even though the current generated by this cell is about 4 times greater than the cell using the MRC U105 anode GDL. This cell also does not show dramatic changes in water content with changing voltages indicating the MRC C anode GDL prevents cell flooding that was observed in the cell using the MRC U105 GDL. While this cell does show a peak in the water content in the cathode GDL, it does not show a corresponding peak in the anode GDL. This lack of high liquid water in the anode GDL is consistent with the higher anode water removal rates observed when using this GDL in 50 cm^2 cells operated at 40 °C.

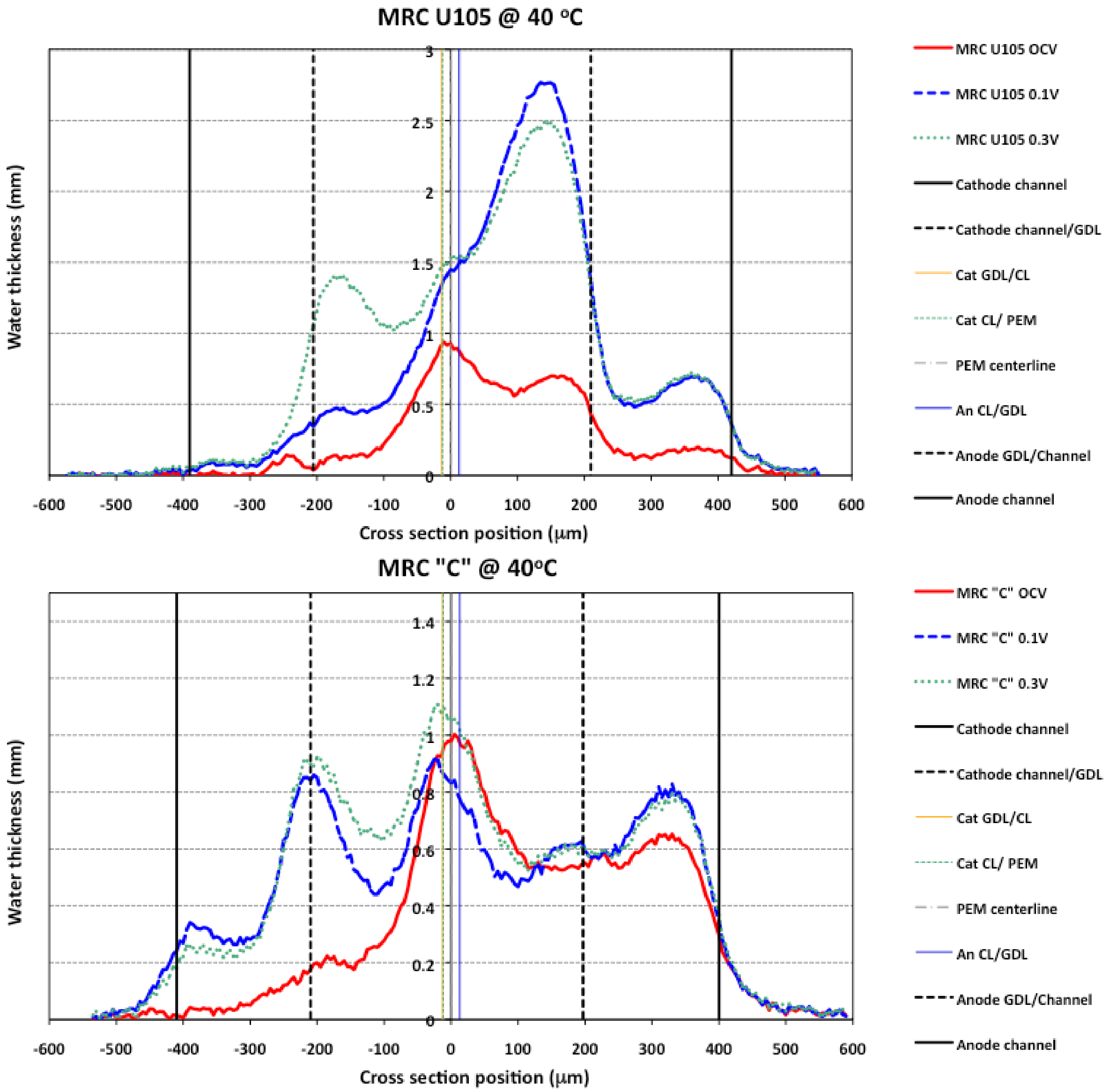

Figure S6 Water profiles of the PEFCs with a) MRC U105 and b) MRC C anode GDLs operated at 40°C at different voltages. Cathode locations correspond to cross-section positions less than zero.

The data at 80°C clearly confirms that the GDL liquid water content is zero when operated at OCV. However, the presence of liquid water in the 40°C and OCV illustrates the difficulty in removing water at the lower temperature. All experiments were performed for up to 1 hour which was sufficient to reach steady state as indicated by the unchanging water profiles over the last 15 minutes of the experiment. The data in figure S6 showing the anode GDL water content being similar at OCV and at 0.3V is real. This just shows that in these cells, the anode GDL saturation does not change with current density while the cathode GDL saturation increases with current density. In fact, the anode GDL water saturation under OCV is similar for both the U105 and MRC C GDLs indicating that at OCV there is liquid in the GDLs at 40°C which could be due to variations in temperature, the fact that the gases are at 100% saturation, and the existence of small amounts of residual saturation within the GDLs.

Low-resolution neutron imaging was performed on 50 cm^2 cells with quad-serpentine flow fields. The results revealed that the cell with the MRC C anode GDL showed much more uniform water distribution across the flow field from inlet to outlet than the cell with the MRC U105 anode GDL. The total water content of the cells increased with increasing current density, which is not surprising since flow field water is expected to increase with more liquid water produced at the higher current densities. The water under the lands was also found to increase with increasing current density indicating that cathode flooding is not the limiting factor under the conditions tested. The correlation of increased water content with improving performance could be due to improved proton transport in the electrolyte or the electrode.

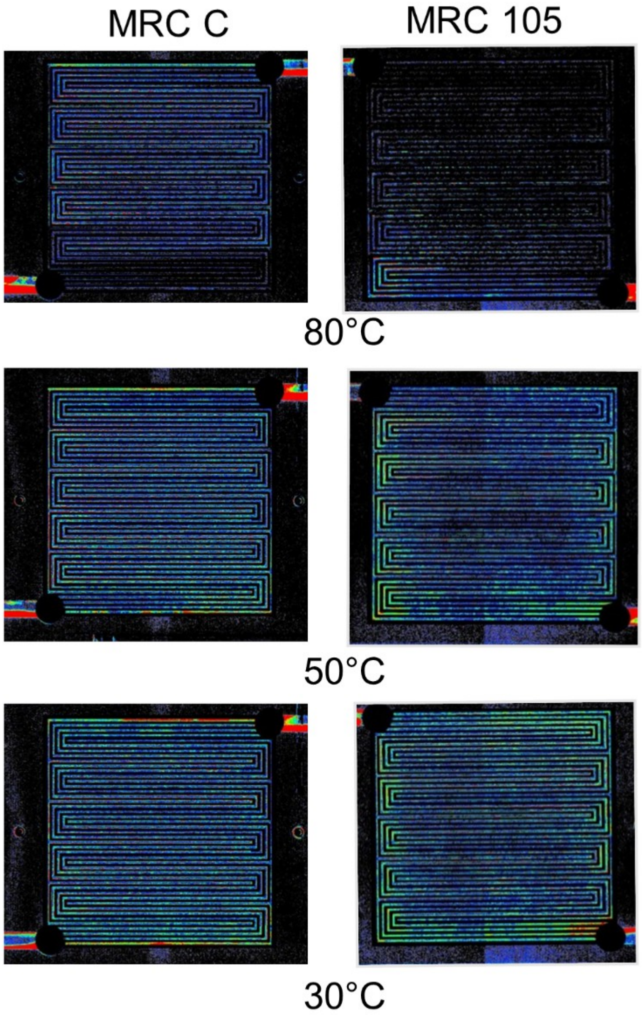

Figure S7 Large-field neutron images for MRC C and MRC U105 at three temperatures: 80 (top), 50 (middle), and 30°C (bottom). Cell area 50 cm^2 (7.07 x 7.07 cm).

GDL Transport Properties Diagnostics

A summary of the comparisons of the GDLs and several of the properties (see details below) are given in Table S2.

Table S3. Summary table of representative material properties for the two GDLs studied.

	MRC 105	**MRC C**
Thickness of uncompressed GDLs (µm)	194 ±11	186±5
Porosity for 18 % compression, (-)	0.70	0.76
Average pore diameter for 15-18 % compression (µm)	11	11
Thermal conductivity ($Wm^{-1}K^{-1}$)	0.12	0.2
Young's Modulus (MPa)	5.9	1.6
Power law exponent for effective diffusivity, n, $g(s) = (1 - s)^n$	4	2.8

Figure S8 shows the set-up for thermal conductivity measurements, where the insulation is removed to show the stainless steel pistons, copper plates and thermocouple locations. Equivalent circuit for resistance calculations is shown as well.

Optical micrographs for MRC U105 and MRC C are shown by Figure S9 and reveal preferential alignment of fibers for MRC C and also a banded structure of this type of GDL. The brighter regions on the micrograph show the regions of low fiber density, whereas the darker bands correspond to the regions of denser fibers and lower porosity.

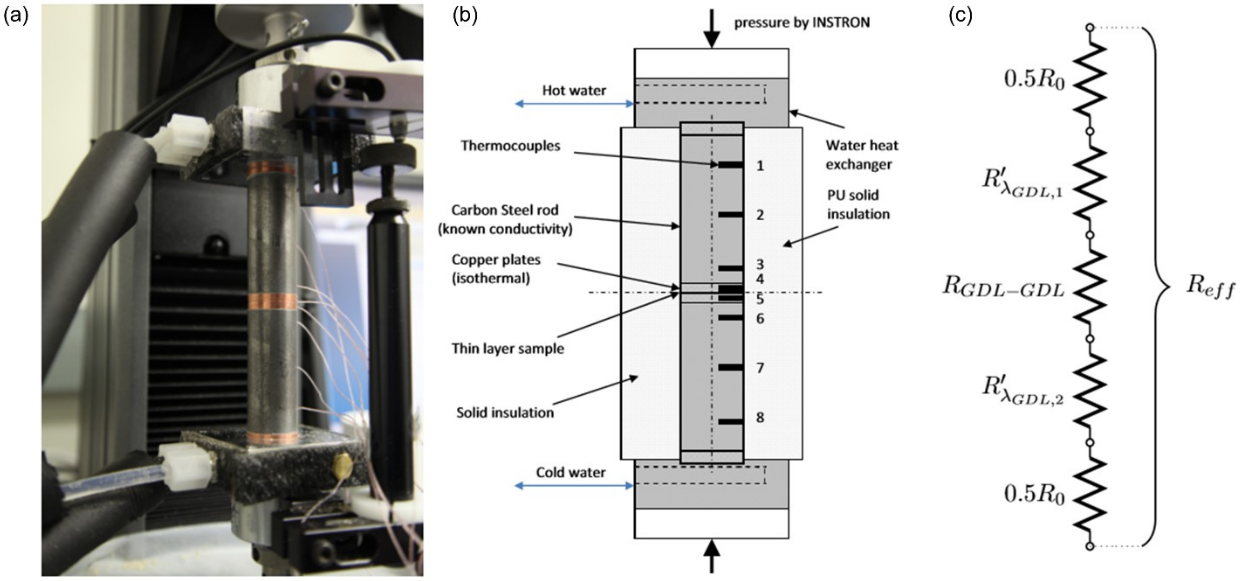

Figure S8 Experimental setup for thermal resistance measurement: a) photograph of the set-up, b) schematic with all the labels and c) equivalent circuit to compute effective resistance.

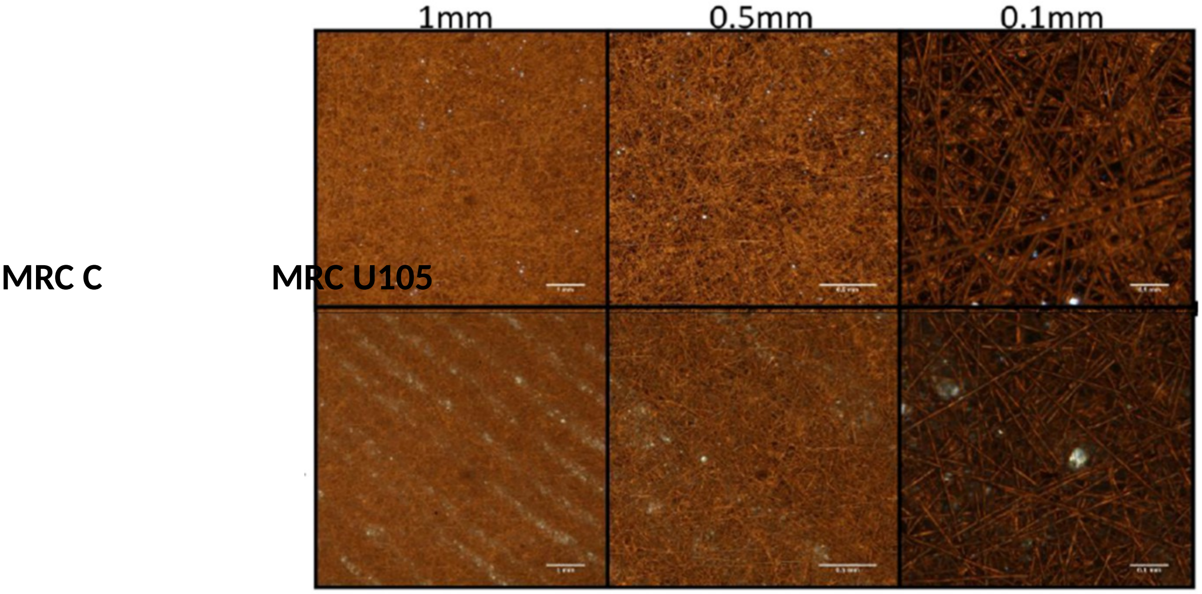

Figure S9 Optical micrographs of MRC C and MRC U105 GDLs where labels at top corresponds to dimensions of scale bars.

Water retention curves are shown by Figure S10 for MRC C and MRC U105 being either untreated or PTFE-treated. For untreated MRC C at zero capillary pressure saturation is 0.2, whereas for PTFE-treated it is close to 0. For MRC U105 saturation is 0.15 for untreated at zero capillary pressure and 0.04 for PTFE-treated. For MRC C at higher saturations and higher capillary pressures the two curves overlap, whereas for MRC U105 PTFE-treatment introduces higher resistance for water removal.

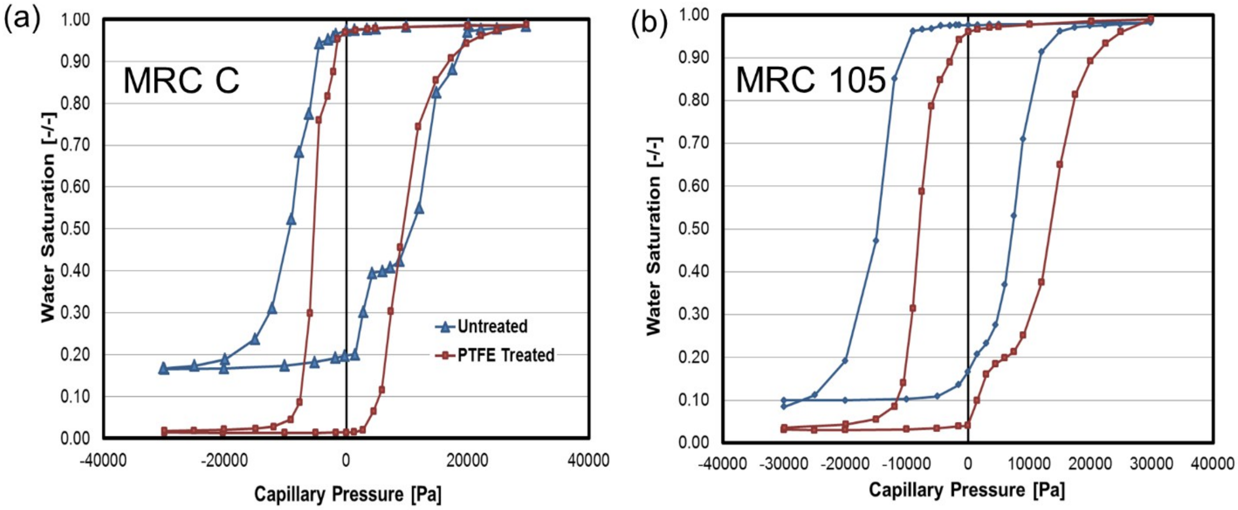

Figure S10 Water retention curves for untreated and PTF-treaded a) MRC C and b) MRC U105 GDLs.

The effective diffusivities for MRC C and MRC U105 for various levels of saturation are shown by Figure S11, where g(s) is obtained by normalizing the measured diffusivities by the dry diffusivity of the GDLs, where saturation is zero. The diffusivity for MRC C decreases less steeply compared to that of MRC U105, as shown by power law fit exponents:

$$g(s) = (1 - s)^n$$

Where s is saturation, and n is power-law exponent, where for MRC C it is 2.8 and for MRC U105 it is 4.

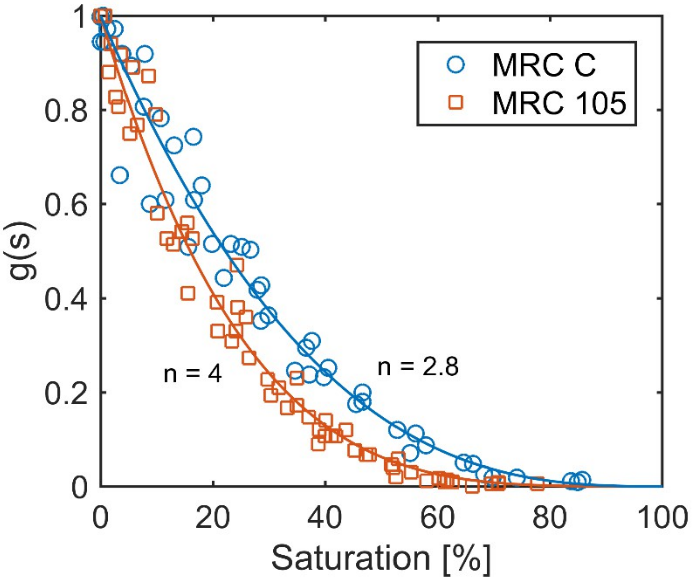

Figure S11. Normalized saturation function, g(S), as a function of liquid saturation for MRC C and MRC U105. The power law fits are shown too.

Porosity distribution for various levels of compression was explored for MRC C and MRC U105 using X-ray CT and shown by Figure S12. In-plane porosity for MRC U105 showed no apparent pattern and preserved its shape at compressions range between 3 and 52 %. The cross-section tomographs for 3 % and 52 % are shown by Figure S12a (bottom of the plot), where void space is significantly reduced for higher compression. For MRC C fiber density modulation is clearly observed qualitatively by cross-section tomographs and quantitatively by calculating void fraction as shown by Figure S12b. The change in porosity between the regions of high and low fiber density are between 0.06 at low compression to more pronounced of 0.08 at high compression. Upon compression the regions with denser fibers absorb most of the stress resulting in even lower porosity.

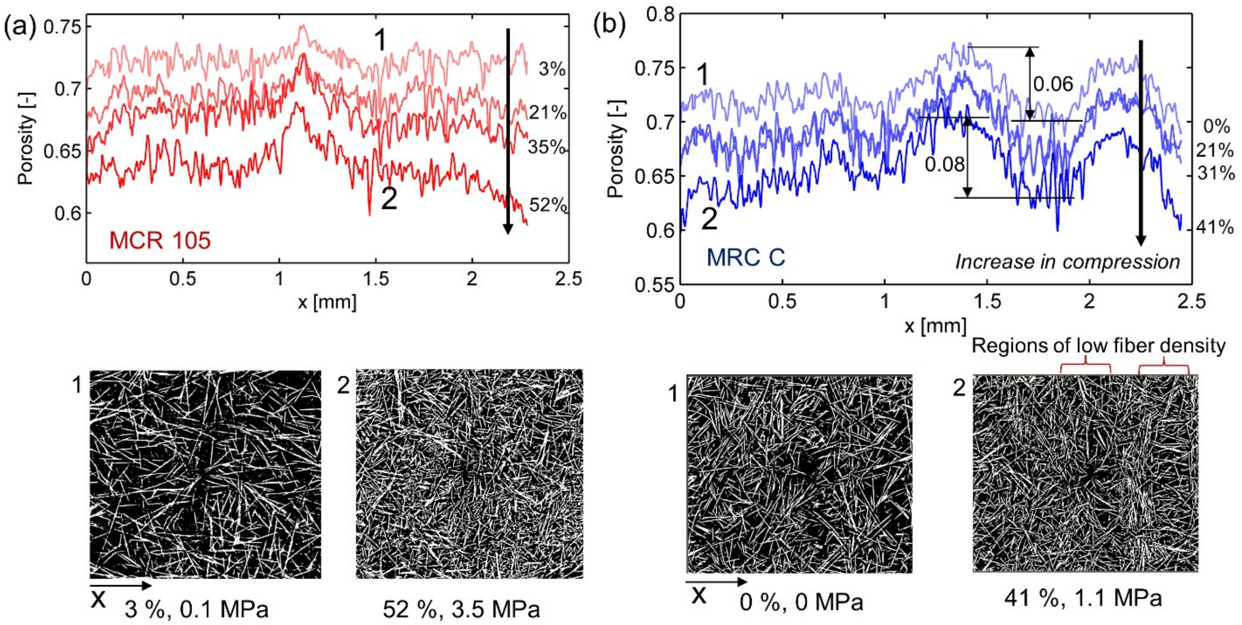

Figure S12 In-plane porosity distribution for various compression levels for a) MRC U105 and b) MRC C . The cross-section tomographs at two compression levels for each GDL are shown on the bottom.

Figure S13a and b shows PDF for MRC C and MRC U105 obtained with MIP and X-ray CT, respectively for a full range of radii. The PDF from the micro X-ray CT data was obtained using spherical kernel fitting algorithm, as reported in-detail in our previous work.[51] From the MIP a peak is observed at radius of 12.3 µm for MRC U105 and a smaller peak at 25 µm, whereas for MRC C these peaks were closer together at 14 and 21 µm. From the X-ray CT a unimodal distribution was observed for both layers with a peak at around 10 µm. Due to the large tail of the distribution that the MIP captures, which is primarily due to large interfacial voids, a computation of mean radius is not accurate from this technique, as it over approximates the mean radius. The mean radii from MIP can be computed from Figure S13c, where it is evident that for MRC U105 it is around 10 µm, whereas for MRC C it is 15 µm. Upon compression from X-ray CT data two types of GDLs showed very similar shift in pore-size distribution, which is shown by Figures S14d, Figure S14 and Figure S15, where in the later the mean radius of the distribution is plotted versus the strain. Figure S14 shows the pore-size distributions for both GDLs. We reported the pore-size distribution for MRC U105 previously,[51] here we show the distributions in two half-GDL thickness domains. The MRC U105 shows very similar distributions for two domains indicating that there is not much through-thickness homogeneity, whereas MRC C showed more through-thickness heteregeneity. From Figure S14, what is interesting is that at all levels of compression MRC C showed higher porosity compared to MRC U105, as shown by Figure S15a.

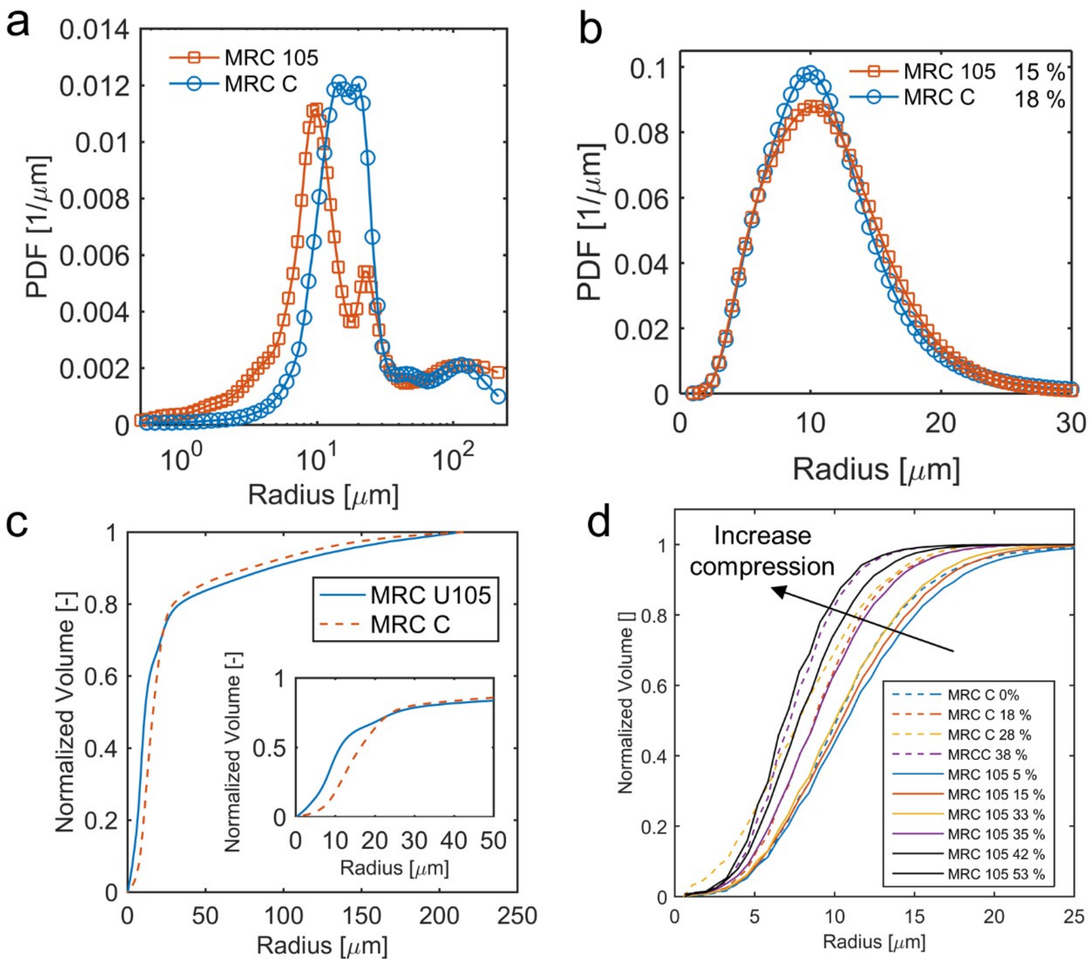

Figure S13 a) PDF obtained with MIP for MRC C and MRC U105 for a full range of radii. b) the PDFs for the two GDLs with X-ray CT, c) the normalized volume for MRC U105. The normalized volume for various compression levels for MRC U105 and MRC C is shown by plot b.

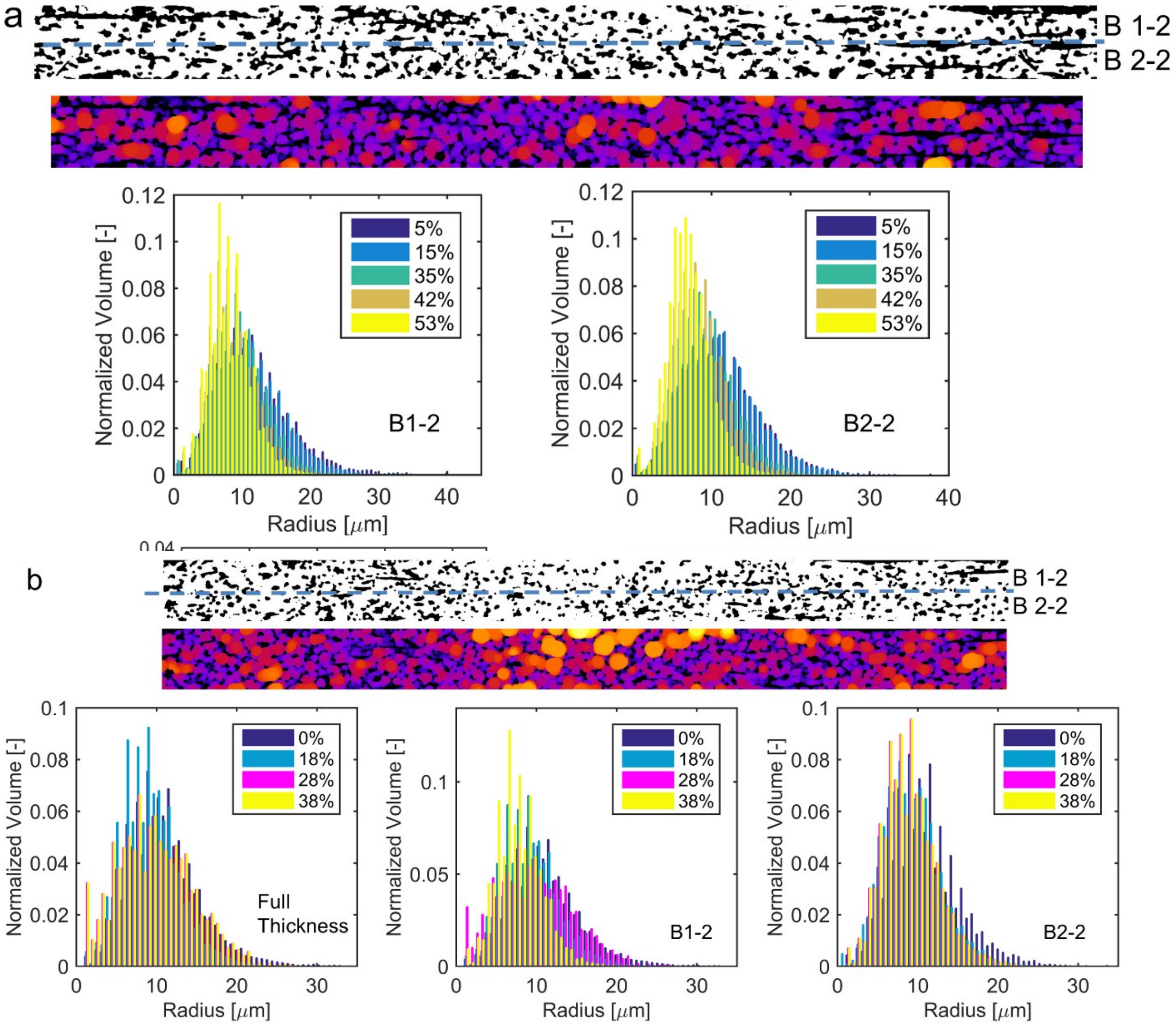

Figure S14 Normalized volume as a function of radius for two representative volumes for a) MRC U105 and b) MRC C.

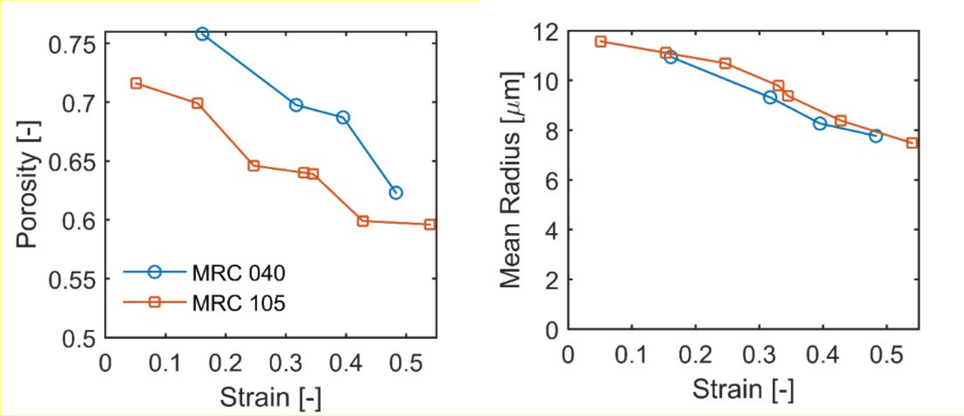

Figure S15 a) Porosity and b) mean radius as a function of strain extracted from X-ray CT data for MRC O40 and MRC U105.

Figure S16 shows the pore-size distributions for two compression levels for the fibre regions of high- and low-density. For uncompressed layer the differences in average radii of fiber-dense and pore-dense regions is not major, however, for high levels of compression (38 %), the mean radii are significantly different, as most of the stress is observed by the fiber-dense regions. This was also observed by Figure S12, where the local porosity fluctuations increased upon compression.

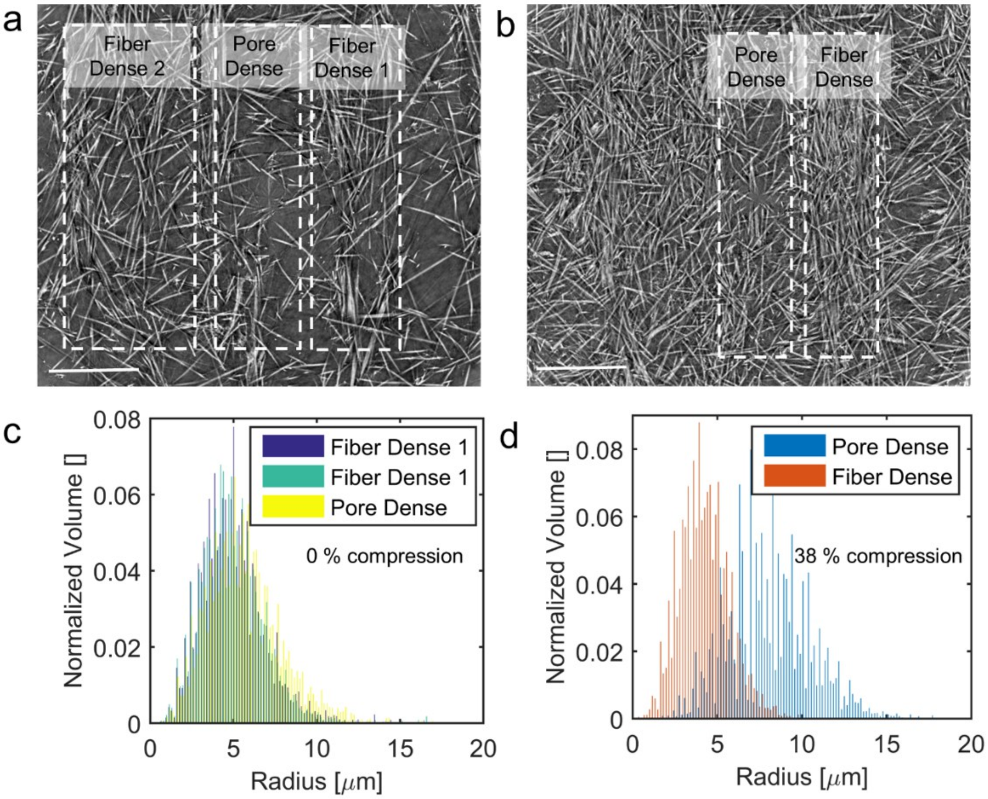

Figure S16. Regions for high and low fiber density regions for which the pore-size distributions are obtained for MRC C for a) uncompressed and b) 38 % compression. The pore-size distributions for these two cases are shown by c and d.

Figure S17 shows volume-averaged saturation for levels of liquid pressures for GDLs at various compression levels. MRC U105 shows monotonic increase in saturation with increased in liquid pressure. Furthermore, with increased compression liquid saturation is reduced for the same liquid pressure. In contrast, MRC C shows significant sample-to-sample variability, primarily due to fiber-density modulations. Either water finds a pathway into high porosity regions at low pressures and then the saturation increases steeply, or water fills the interface between the GDL and sample holder without finding the path to higher porosity regions. The key observed for 29% compression is also seen in water retention curves for MRC C shown by Figure S10.

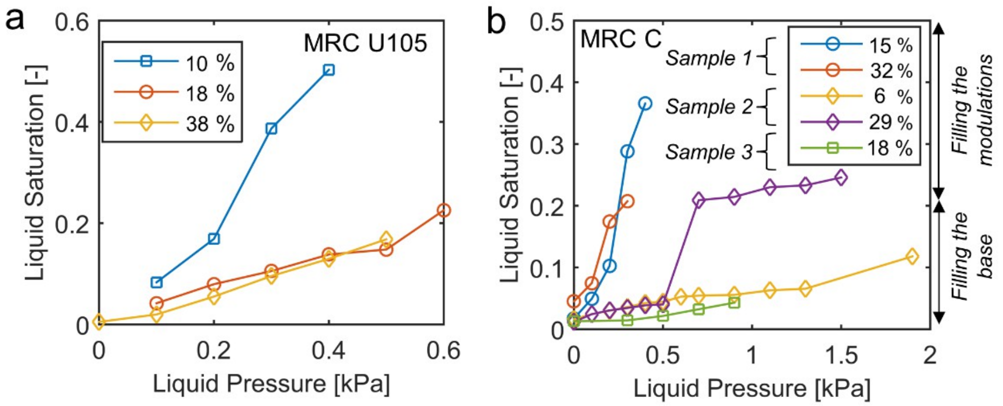

Figure S17. Water retention curves obtained with X-ray CT for various compression levels for a) MRC U105 and b) MRC C.

Studies with alternate anode GDL

Figure S18 shows distributions of pore structure from a different GDL (X0155) that likewise contains fiber-density modulations. From (a,b), one can see modulations on the order of 20 percent that remain even after compression. Liquid infiltration studies demonstrate that liquid water moves preferentially through the low density regions (d). Furthermore, this is associated in (c) with better performance observed by the GDLs when different amounts of PTFE overcoats are added. The detachment velocity for the X0155 GDL in (e) is lower than the baseline GDL (see Figure 5c), which his consistent with the findings in the rest of the article. There is also a smaller effect due to MPL loading and orientation of the GDL.

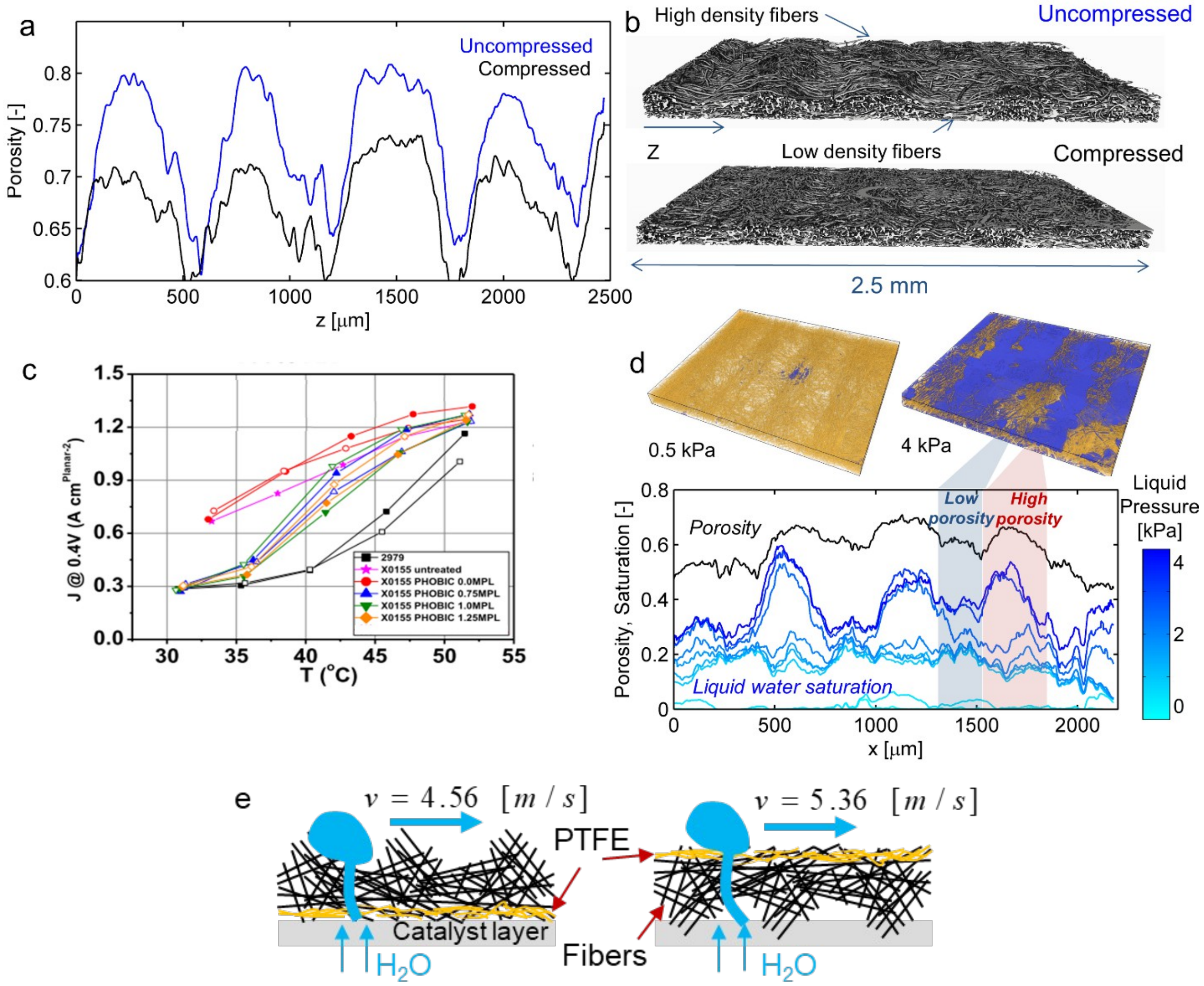

Figure S18. (a) Porosity, (b) XCT images of dry and compressed GDL containing fiber-density modulations. (d) water flow and distributions through the GDL. (c) Polarization curves with the GDLs with different MPL thicknesses. (d) Detachment velocity for different GDL orientations.